



1 **Measurement Report: Distinct size dependence and**
2 **diurnal variation of OA hygroscopicity, volatility, and**
3 **CCN activity at a rural site in the Pearl River Delta**
4 **(PRD) region, China**

5 Mingfu Cai^{1,2,3}, Shan Huang^{1,2*}, Baoling Liang⁴, Qibin Sun⁴, Li Liu^{5*}, Bin Yuan^{1,2},
6 Min Shao^{1,2}, Weiwei Hu⁶, Wei Chen⁶, Qicong Song^{1,2}, Wei Li^{1,2}, Yuwen Peng^{1,2},
7 Zelong Wang^{1,2}, Duohong Chen⁷, Haobo Tan⁵, Hanbin Xu⁴, Fei Li⁵, Xuejiao Deng⁵,
8 Tao Deng⁵, Jiaren Sun³, and Jun Zhao^{4,8,9}

9 ¹ Institute for Environmental and Climate Research, Jinan University, Guangzhou, Guangdong
10 511443, China

11 ² Guangdong-Hongkong-Macau Joint Laboratory of Collaborative Innovation for Environmental
12 Quality, Guangzhou, Guangdong 511443, China

13 ³ Guangdong Province Engineering Laboratory for Air Pollution Control, Guangdong Provincial
14 Key Laboratory of Water and Air Pollution Control, South China Institute of Environmental
15 Sciences, MEE, Guangzhou, Guangdong 510655, China

16 ⁴ School of Atmospheric Sciences, Guangdong Province Key Laboratory for Climate Change and
17 Natural Disaster Studies, and Institute of Earth Climate and Environment System, Sun Yat-sen
18 University, Zhuhai, Guangdong 519082, China

19 ⁵ Institute of Tropical and Marine Meteorology of China Meteorological Administration, Guangzhou
20 510640, China

21 ⁶ State Key Laboratory of Organic Geochemistry and Guangdong Key Laboratory of Environmental
22 Protection and Resources Utilization, Guangzhou Institute of Geochemistry, Chinese Academy of
23 Sciences, Guangzhou 510640, China

24 ⁷ Guangdong Environmental Monitoring Center, Guangzhou 510308, China

25 ⁸ Southern Marine Science and Engineering Guangdong Laboratory (Zhuhai), Zhuhai, Guangdong



- 26 519082, China
- 27 ⁹ Guangdong Provincial Observation and Research Station for Climate Environment and Air Quality
- 28 Change in the Pearl River Estuary, Guangzhou, Guangdong 510275, China
- 29 *Corresponding authors: Shan Huang (shanhuang_eci@jnu.edu.cn) and Li Liu (liul@gd121.cn)



30 **Abstract.**

31 Organic aerosol (OA) has a significant contribution to cloud formation and hence climate
32 change. However, high uncertainties still exist in its impact on global climate, owing to the varying
33 physical properties affected by the complex formation and aging processes. In this study, the
34 hygroscopicity, volatility, cloud condensation nuclei (CCN) activity, and chemical composition of
35 particles were measured using a series of online instruments at a rural site in the Pearl River Delta
36 (PRD) region of China in Fall 2019. During the campaign, the average hygroscopicity of OA (κ_{OA})
37 increased from 0.058 at 30 nm to 0.09 at 200 nm, suggesting a higher oxidation state of OA at larger
38 particle sizes, supported by a higher fraction of extremely low volatile OA (ELVOA) for larger size
39 particles. Significantly different diurnal patterns of κ_{OA} were observed between Aitken mode and
40 accumulation mode. For Aitken mode (30-100 nm), the κ_{OA} values showed daily minima (0.02-0.07)
41 during daytime, while exhibited a daytime peak (~ 0.09) in the accumulation mode. Coincidentally, a
42 daytime peak was observed for both aged biomass burning organic aerosol (aBBOA) and less
43 oxygenated organic aerosol (LOOA) based on source apportionment, which were attributed to the
44 aging processes and gas-particle partitioning through photochemical reactions. In addition, the
45 fraction of semi-volatile OA (SVOA) was higher at all measured sizes during daytime than during
46 nighttime. These results indicate that the formation of secondary OA (SOA) through gas-particle
47 partitioning can generally occur at all diameters, while the aging processes of pre-existing particles
48 are more dominated in the accumulation mode. Furthermore, we found that applying a fixed κ_{OA}
49 value (0.1) could lead to an overestimation of the CCN number concentration (N_{CCN}) up to 12%-
50 19% at 0.1%-0.7% supersaturation (SS), which was more obvious at higher SS during daytime.
51 Better prediction of N_{CCN} could be achieved by using size-resolved diurnal κ_{OA} , which indicates that



52 the size-dependence and diurnal variations of κ_{OA} can strongly affect the N_{CCN} at different SS. Our
53 results highlight the need for accurately evaluating the atmospheric evolution of OA at different size
54 ranges, and their impact on the physicochemical properties and hence climate effects.

55

56 1. Introduction

57 The impact of aerosol particles on global climate is widely known, including absorbing and
58 scattering solar radiation, and acting as cloud condensation nuclei (CCN). However, the extent of
59 their contribution on the climate forcing is still unclear. Organic aerosol (OA) as a dominant
60 component of fine particles (Jimenez et al., 2009), may contribute the uncertainties of climate effects
61 of particles, mainly owing to unknown sources, physical properties, formation, and aging
62 mechanisms (Volkamer et al., 2006; Kuang et al., 2020b; Rastak et al., 2017). Numerous studies show
63 that secondary organic aerosol (SOA) accounts for a large OA fraction in most atmospheric
64 environments (e.g., Huang et al., 2014; Shrivastava et al., 2017; Kanakidou et al., 2005; Hallquist et
65 al., 2009). Nevertheless, both primary OA (POA) and SOA in the ambient air remain poorly
66 characterized in terms of the formation mechanism and atmospheric evolution, and their particle
67 diameter can vary on a large scale. Their impact on the global climate and atmospheric chemistry is
68 still highly uncertain.

69 A combination of Aerodyne Aerosol Mass Spectrometer (AMS) or Aerosol Chemical Species
70 Monitor (ACSM) with positive matrix factorization (PMF) is widely used for investigating the OA
71 evolution in the atmosphere (Li et al., 2013; Huang et al., 2018; Huang et al., 2014; Chen et al.,



72 2015;Jimenez et al., 2009). For instance, Qin et al. (2017) found that hydrocarbon-like OA (HOA)
73 from traffic emission contributed up to 40% of OA during nighttime, owing to daytime traffic
74 restrictions on heavy vehicles in urban Guangzhou. Kuang et al. (2020a) reported a dominant
75 contribution to oxygenated OA (OOA) through aqueous-phase reaction in the North China Plain
76 (NCP). Guo et al. (2020) observed different SOA mechanisms between clean and pollution episodes
77 in the Pearl River Delta (PRD) region. Nevertheless, the investigation of bulk OA is still insufficient
78 in understanding the aerosol climate effects without the size-resolved characterization. The OA size
79 distribution is largely dependent on its composition, sources and aging level. Li et al. (2012)
80 observed various mass distribution patterns for different species in airborne particulate organics and
81 reported that dehydrated sugars, fossil fuel-derived *n*-alkanes, and PAHs showed a unimodal
82 distribution, while non-dehydrated sugars and plant was derived as *n*-alkanes which presented a
83 bimodal pattern. In the urban region, Aitken mode was mainly dominated by HOA owing to traffic
84 emissions (Zhang et al., 2005b;Cai et al., 2020). In the marine atmosphere, the size distribution of
85 fine mode POA was found to be independent of sea salt, while coarse mode particles tended to be
86 internally mixed with sea salt (Gantt and Meskhidze, 2013). Similarly, the OA physical properties
87 were also found to be size-dependent. Deng et al. (2018) reported a higher OA hygroscopicity
88 ($\kappa_{OA} \approx 0.22$) at about 150 nm than that ($\kappa_{OA} \approx 0.19$) at sub-100 nm. In contrast, Zhao et al. (2015)
89 found that κ_{OA} decreased from 0.17 at 50 nm to 0.07 at 200 nm in laboratory study, which was
90 attributed to the higher oxidation degree for smaller particles.

91 The size dependence of OA properties in the aforementioned studies might exert impact on the
92 CCN prediction, which is mainly determined by their sources and formation processes. Cai et al.
93 (2018) found that N_{CCN} at 0.1% SS was underestimated by about 10% if a κ_{OA} value of 0.1 was used.



94 A model simulation from Liu and Wang (2010) showed that an increase of about 40-80% for the
95 CCN concentration was obtained by increasing the κ value of POA from 0 to 0.1. Wang et al. (2008)
96 reported that the uncertainties of the first indirect aerosol effect varied from -0.2 to 0.2 W m^{-2} for a
97 κ_{OA} value of 0 to 0.25. Rastak et al. (2017) showed that using a single-parameter framework of κ_{OA}
98 in evaluating the climate effects of aerosol could lead to significant errors (about -1.02 W m^{-2}),
99 which is the same order as the climate forcing of anthropogenic aerosol during the industrial period.
100 These results further highlight a need for the understanding of the relationship between the OA
101 evolution processes and its impact on the CCN activity at different particle sizes.

102 The OA hygroscopicity and volatility can provide information about the evolution of OA, given
103 that they are often related to the chemical composition of the particles. A positive correlation
104 between the hygroscopicity values and the oxidation degree of OA, including the ratio of atomic
105 oxygen to atomic carbon (O:C), the oxidation state ($\overline{\text{OS}}_{\text{C}}$), or the mass fraction of m/z 44 (for CO_2^+)
106 ion fragments in the organic spectra (f_{44}) from chemical composition, were widely reported in the
107 literature (Wu et al., 2013; Pajunoja et al., 2015; Chang et al., 2010). Kim et al. (2020) found that the
108 κ_{OA} was positively and negatively correlated with OOA and HOA at different size ranges,
109 respectively. Deng et al. (2019) reported a decreasing trend of κ_{OA} at a size range of 100-360 nm
110 during daytime in a forest environment, suggesting the formation of biogenic SOA (BSOA) through
111 photochemical oxidation of biogenic volatile organic compounds (BVOCs). The OA volatility,
112 specifically saturation vapor concentration (C^*), is linked to the gas-particle partitioning and aging
113 processes. In general, the C^* value decreases with an increase of the oxidation degree and the
114 number of atomic carbon (Donahue et al., 2011). May et al. (2013) found that most of the biomass-
115 burning POA were semi-volatile. Saha et al. (2017) showed a lower volatility of OA in the afternoon



116 hours using a dual-thermodenuder (TD) system, probably owing to photochemical oxidation of OA.
117 Hong et al. (2017) derived the OA volatility distribution by a combination of the VTMDA
118 measurement and a multi-component evaporation dynamics model, and found a moderate ($R \approx 0.4$)
119 correlation between the OA groups obtained by the VTMDA data and the PMF results, respectively.

120 In this study, we investigate physical properties of OA at different size ranges, and evaluate
121 their influence on the atmospheric CCN concentration. A rural field measurement was conducted at
122 the Heshan site in the Pearl River Delta (PRD) region, China, during Fall 2019 (October and
123 November). The hygroscopicity, volatility, size-resolved CCN activity, and chemical composition
124 were measured by a series of online instruments. The size-resolved hygroscopicity and volatility
125 distribution of organics was investigated. PMF was employed to analyze the sources and processes
126 of OA. The impact of diurnal variation and size dependence of κ_{OA} on the N_{CCN} prediction at
127 different supersaturation (SS) was assessed.

128 2. Measurement and methodology

129 2.1 Measurement site

130 The field measurements were conducted at the Heshan supersite in the Guangdong province,
131 China during autumn time 2019 (27th September to 17th November 2019). This supersite (22°42'39.
132 1"N, 112°55'35.9"E) is located at the southwest of the PRD region and surrounded by farms and
133 villages, with an altitude of about 40 m. All sample particles first passed through a Nafion dryer
134 (Model MD-700, Perma Pure Inc., USA) to maintain a relative humidity (RH) lower than 30%. The
135 schematic diagram of the experimental setup can be found in Fig. S1. Detailed descriptions of the



136 measurement site and some instruments can be found in Cai et al. (2021a).

137 2.2 Instrumentation

138 2.2.1 Aerosol hygroscopicity and volatility measurement

139 Size-resolved hygroscopicity and volatility of particles were measured by a H/V-TDMA
140 (model M3000, Bmet Inc., China). The instrument consists of two differential mobility analyzers
141 (DMA1 and DMA2, model 3081 L, TSI Inc., USA), a Nafion humidifier (Model MD-700, Perma
142 Pure Inc., USA), a heater tube, and a condensation particle counter (CPC, model 3788, TSI Inc.,
143 USA). The instrument was operated in H- and V- mode during the measurement with a cycle time
144 of about 3-4 h. The dried sample particles were firstly charged by an X-ray neutralizer and then
145 classified by DMA1 at six diameters (30, 50, 80, 100, 150, and 200 nm). In the H-mode, the chosen
146 particles with a specific dry diameter (D_0) were sequentially humidified by the Nafion humidifier
147 to achieve 90% of RH. A combination of DMA2 and CPC were employed to measure the size
148 distribution of humidified particles (Dp_{wet}). The hygroscopic growth factor (GF) at a certain dry
149 diameter can be defined as:

$$150 \quad GF(D_0) = \frac{Dp_{wet}}{D_0} \quad (1)$$

151 In the V-mode, the selected particles from DMA1 were heated in the heater tube at 100, 150,
152 200, and 250°C, respectively. Similar to the H mode, the size distribution of heated particles along
153 with particles at room temperature (25°C) was measured by the DMA2 and CPC. The volatility
154 shrink factor (VSF) at a certain diameter and temperature is then defined as:

$$155 \quad VSF(T, D_0) = \frac{Dp(T)}{D_0} \quad (2)$$

156 Before the campaign, standard polystyrene latex spheres (PSLs; with a size of 20, 50, and 200



157 nm), ammonium sulfate, and sodium chloride were used to calibrate the diameter classification of
158 DMAs, hygroscopicity measurement, and the transport efficiency of particles in the heater tube,
159 respectively. For the H/V-TDMA data, the TDMAfit algorithm (Stolzenburg and McMurry, 2008)
160 was applied to fit the growth factor and volatility shrink factor probability density function (GF-
161 PDF and VSF-PDF) with various DMA transfer functions. The detailed data inversion processes
162 can be found in Tan et al. (2013a).

163 **2.2.2 The size-resolved CCN activity and particle number size distribution measurement**

164 A combination of a cloud condensation nuclei counter (CCNc, model 200, DMT Inc., USA)
165 and a scanning mobility particle sizer (SMPS, model 3938L75, TSI Inc., USA) was employed to
166 measure size resolved CCN activity. The supersaturation (SS) of each column (A and B) of CCNc
167 was set to be 0.1%, 0.2% and 0.4% (for column A), and 0.7%, 0.9% and 1.0% (for column B),
168 respectively. During the measurement, the SMPS was operated at a scanning mode. The sample
169 particles were firstly neutralized by an X-ray neutralizer (model 3088, TSI Inc., USA) and were
170 subsequently classified by a DMA. The classified particles were then split into three paths: one to a
171 CPC (model 3756, TSI Inc., USA) for measurement of particle number concentration (with a flow
172 rate of 0.6 LPM) and two to the CCNc for measurement of the CCN number concentration (N_{CCN})
173 at a specific SS (with a flow rate of 0.5 LPM).

174 The particle number size distribution in a size range of 1 nm-10 μm was measured by a suite of
175 instruments including a diethylene glycol scanning mobility particle sizer (DEG-SMPS, model
176 3938E77, TSI Inc., USA), a SMPS (model 3938L75, TSI Inc., USA), and an aerodynamic particle
177 sizer (APS, model 3321, TSI Inc., USA). The detailed description of these instruments can be found



178 in Cai et al. (2021a). Before the measurement, the SMPSs were calibrated with PSLs (20, 50 and
179 200 nm) and the CCNc was calibrated with ammonium sulfate ((NH₄)₂SO₄) particles at selected SSs
180 (0.1%, 0.2%, 0.4%, 0.7%, 0.9%, and 1.0%).

181 **2.2.3 Aerosol chemical composition measurement**

182 The size-resolved chemical composition of ambient aerosol particles was measured by a soot
183 particle aerosol mass spectrometer (SP-AMS, Aerodyne Research, Inc., USA). The principle and
184 operation of the instrument are generally the same as a high resolution time-of-flight aerosol mass
185 spectrometer (HR-ToF-AMS) (Canagaratna et al., 2007). In addition to an original tungsten
186 vaporizer (~600°C), a soot-particle module which mainly contains a Nd:YAG (1064 nm) laser was
187 integrated into HR-ToF-AMS for vaporizing refractory species (Onasch et al., 2012). As a result,
188 SP-AMS can provide chemical information for non-refractory species (nitrate, sulfate, ammonium,
189 chloride, and organics) as well as refractory species such as refractory black carbon (rBC) and
190 several metals. During the campaign, SP-AMS was run between V mode (only tungsten vaporizer)
191 and SP mode (tungsten and laser vaporizers) with a time resolution of 1 min. In order to minimize
192 disturbance caused by mode switch, 15 min averaged data are used in the present study. More details
193 on the quantification using ionization efficiency, composition dependent collection efficiency and
194 external instrument as well as software for SP-AMS data analysis could be found in Kuang et al.
195 (2021).

196 Facilitated by the time-of-flight chamber in SP-AMS, the particle mass size distribution can be
197 measured in submicrometer size range, specifically, 40 to 800 nm in vacuum aerodynamic diameter
198 (D_{va}). The mass size distribution for relevant AMS species was used in this study for investigating



199 the link between particle chemical composition and volatility/hygroscopicity. Since SP-AMS
200 provided the size distribution versus D_{va} , the equation below was used to convert D_{va} into mobility
201 diameter (D_p).

$$202 \quad D_p = \frac{D_{va}}{S \times \frac{\rho_p}{\rho_0}} \quad (3)$$

203 where S is the shape factor, ρ_p is the particle density, and ρ_0 is the density for water (1 kg m^{-3}). In
204 this study, we estimate that the particles were close to sphere due to high RH in the PRD and thus a
205 shape factor of 0.8 was applied. An overall particle density of 1.6 kg m^{-3} is used.

206 Based on high resolution data from SP-AMS, source apportionment was performed for organic
207 aerosols (OA) in the bulk PM_{10} with positive matrix factorization (PMF, Paatero, 1997; Paatero and
208 Tapper, 1994) following the instruction in Ulbrich et al., 2009. The input data, selection of solutions,
209 mass spectral profile, and time series of each factor can be found in Kuang et al. (2021). In brief,
210 OA measured at the Heshan site could be divided into six components with identified sources and
211 processes, including two from primary sources and four factors corresponding to secondary
212 formation: a hydrocarbon-like OA (HOA) contributed mainly by vehicle exhausts mixed with
213 cooking emissions, a biomass burning OA (BBOA) related to biomass burning combustion from the
214 surrounding villages, an aged BBOA (aBBOA), a more oxygenated OA (MOOA) from regional
215 transport, a less oxygenated OA (LOOA) provided by daytime photochemical formation, and a
216 nighttime-formed OA (Night-OA) related to secondary formation during nighttime.

217 2.3 Methodology

218 2.3.1 Estimates of hygroscopicity

219 The hygroscopicity parameter κ can be obtained under subsaturation condition by the H/V-



220 TDMA measurement and supersaturation condition by the CCNc measurement. The κ value
221 (κ_{HTDMA}) can be estimated from the growth factor measured by H/V-TDMA (Petters and
222 Kreidenweis, 2007):

$$223 \quad \kappa_{\text{HTDMA}} = (\text{GF}^3 - 1) \left[\frac{1}{\text{RH}} \exp \left(\frac{4\sigma_{\text{s/a}} M_{\text{w}}}{RT\rho_{\text{w}} D_{\text{p}}} - 1 \right) \right] \quad (4)$$

224 where $\sigma_{\text{s/a}}$ is the surface tension of the solution/air interface and the solution is temporarily assumed
225 to be pure water (0.0728 N m^{-1} at 298.15 K), M_{w} is the molecular weight of water ($0.018 \text{ kg mol}^{-1}$),
226 R is the universal gas constant ($8.31 \text{ J mol}^{-1} \text{ K}^{-1}$), T is the thermodynamic temperature in Kelvin
227 (298.15 K), ρ_{w} is the density of water (about 997.04 kg m^{-3} at 298.15 K) and D_{p} is the particle
228 diameter in meter.

229 For the CCNc measurement, the κ value (κ_{CCN}) is calculated from the critical supersaturation
230 (S_{c}) and the critical diameter (D_{50}) by the following equation (Petters and Kreidenweis, 2007):

$$231 \quad \kappa_{\text{CCN}} = \frac{4A^3}{27D_{50}^3 (\ln S_{\text{c}})^2}, A = \frac{4\sigma_{\text{s/a}} M_{\text{w}}}{RT\rho_{\text{w}}} \quad (5)$$

232 The critical diameter, D_{50} , is defined as the diameter at which 50% of the particles are activated
233 at a specific SS, and can be obtained from the N_{CCN} and N_{CN} measured by the CCNc and SMPS
234 system:

$$235 \quad \frac{N_{\text{CCN}}}{N_{\text{CN}}} = \frac{B}{1 + \left(\frac{D_{\text{p}}}{D_{50}}\right)^c} \quad (6)$$

236 where the B and C are fitting coefficients.

237 2.3.2 Derivation of the size-resolved hygroscopicity of organic matter

238 The size-resolved chemical composition is adopted to derive the size-dependent hygroscopicity
239 of organic matter (κ_{OA}). However, the AMS cannot provide sufficient information of the size-
240 resolved species, especially for small size particles ($< 100 \text{ nm}$) owing to the low mass concentration.



241 Thalman et al. (2017) proposed a method to reconstruct the size-resolved chemical composition,
242 which combines a time-resolved bulk mass concentration and an average mass distribution.
243 Nevertheless, the variation of mass distribution was not considered in this method. In this study, a
244 bimodal lognormal distribution function method was adopted and the one-hour average mass
245 distribution was fitted to obtain the reconstructed size-resolved chemical composition. The average
246 mass distribution with bimodal lognormal fitted modes of each species was shown in Fig. S2.

247 According to the ZSR mixing rule (Zdanovskii, 1948; Stokes and Robinson, 1966), the
248 hygroscopicity of particles (κ_{AMS}) can be calculated based on the SP-AMS measurement, assuming
249 an internal mixing state for all particles:

$$250 \quad \kappa_{\text{AMS}} = \sum_i \kappa_i \varepsilon_i \quad (7)$$

251 where κ_i is the κ value of each component and ε_i is the volume fraction of corresponding species in
252 particles. The mole concentrations of the inorganic species are estimated based on the NH_4^+ , SO_4^{2-} ,
253 and NO_3^- measured by the AMS (Gysel et al., 2007):

$$254 \quad n_{\text{NH}_4\text{NO}_3} = n_{\text{NO}_3^-}$$

$$255 \quad n_{\text{H}_2\text{SO}_4} = \max(0, n_{\text{SO}_4^{2-}} - n_{\text{NH}_4^+} + n_{\text{NO}_3^-})$$

$$256 \quad n_{\text{NH}_4\text{HSO}_4} = \min(2n_{\text{SO}_4^{2-}} - n_{\text{NH}_4^+} + n_{\text{NO}_3^-}, n_{\text{NH}_4^+} - n_{\text{NO}_3^-})$$

$$257 \quad n_{(\text{NH}_4)_2\text{SO}_4} = \max(n_{\text{NH}_4^+} - n_{\text{NO}_3^-} - n_{\text{SO}_4^{2-}}, 0)$$

$$258 \quad n_{\text{HNO}_3} = 0 \quad (8)$$

259 where n denotes the number of moles of each component (NH_4^+ , SO_4^{2-} and NO_3^-), ε_{org} and ε_{BC}
260 were obtained from mass concentration measured by the SP-AMS. The density and κ value of each
261 component were listed in Table 1.

262 The κ_{OA} can be calculated based on the size-resolved chemical composition and H/V-TMDA



263 measurement using following equation:

$$264 \quad \kappa_{OA} = \frac{\kappa_{HTDMA} - (\kappa_{inorgsalt} \varepsilon_{inorgsalt} + \kappa_{BC} \varepsilon_{BC})}{\varepsilon_{org}} \quad (9)$$

265 2.3.3 Volatility data

266 During the heating process, some particles could be lost between DMA₁ and DMA₂ due to
267 complete evaporation (CV), thermophoresis, and Brownian diffusion (Philippin et al., 2004).
268 Owing to these losses, the V-mode measurement does not represent the actual volatility distribution
269 of the monodisperse particles. The sodium chloride (NaCl) particles, which do not evaporate at the
270 set temperature in this measurement, were used to determine the particle losses owing to
271 thermophoretic forces and diffusion. The size- and temperature-dependent transmission efficiency
272 ($\eta(D_p, T)$) of NaCl in the heater was shown in Fig. S3. Thus, the number fraction of CV group
273 ($NF_{CV}(D_p, T)$) at a certain diameter and temperature can be calculated using the following equation
274 (Cheung et al., 2016):

$$275 \quad NF_{CV}(D_p, T) = 1 - \frac{N'(D_p, T)}{N(D_p)\eta(D_p, T)} \quad (10)$$

276 where $N'(D_p, T)$ is the number concentration of particles at a specific diameter and temperature
277 after heating, which was measured by the CPC in the H/V-TDMA. The $N(D_p)$ is the number
278 concentration of particles with a diameter D_p before heating, which was provided by the SMPS
279 measurement. The volume fraction remaining (VFR) after heating for the measured particles can be
280 obtained according to the following equation:

$$281 \quad VFR(D_p, T) = \sum_i VSF_i^3(D_p, T) NF_i(D_p, T) [1 - NF_{CV}(D_p, T)] \quad (11)$$

282 where i represents the i th VSF bin, and NF_i is the number fraction of particles with VSF_i , which is
283 calculated based on the VSF-PDF ($c(VSF, D_p, T)$):



$$NF_i = \int_{VSF_i}^{VSF_{i+1}} c(VSF, D_p, T) dVSF \quad (12)$$

The mass fraction remaining (MFR) was assumed to be proportional to VFR, assuming that the density of particles was constant before and after heating.

2.3.4 Multi-component evaporation dynamics model

Based on the volatility basis set (VBS) framework (Donahue et al., 2011), the organic matter was classified into three organic groups based on the saturation concentration ($C^*(T_{ref})$, $T_{ref}=298.15$ K): extremely low volatility organic aerosol (ELVOA, $C^*=10^{-5}$ $\mu\text{g m}^{-3}$), low volatility organic aerosol (LVOA, $C^*=10^{-2}$ $\mu\text{g m}^{-3}$), and semi-volatility organic aerosol (SVOA, $C^*=10$ $\mu\text{g m}^{-3}$).

A multi-component evaporation dynamics model described by Lee et al. (2011) was used to simulate the evaporation of particles in the heated tube of the H/V-TDMA by solving the mass transfer regime equation, in order to obtain the size-resolved distribution of the aforementioned three OA groups. The MFR, residence time (about 4.11 s) in the heater tube, the temperature of the heater tube, particle number concentration, particle sizes, chemical composition, and thermophysical properties of each species (Table 2) were input into the model. The particles were assumed to be internally mixed with organic and inorganic species, including three organic groups, NH_4NO_3 , $(\text{NH}_4)_2\text{SO}_4$, and black carbon (BC). The mass transfer of each component i between the aerosol and gas phases in the transition regime was calculated from the following equation:

$$\frac{dm_{p,i}}{dt} = 2\pi D_i D_p f(Kn, \alpha) (C_{i,g} - f_i C_i^*(T) \exp\left(\frac{A\sigma_s/aM_i}{D_p \rho_i RT}\right))$$
$$\frac{dC_{i,g}}{dt} = -\frac{dm_{p,i}}{dt} N_p(D_p) \quad (13)$$

where $m_{p,i}$ (μg) is the mass of species i in a single particle, $C_{i,g}$ ($\mu\text{g m}^{-3}$) is its gas-phase



305 concentration, D_i ($\text{m}^2 \text{s}^{-1}$) is the diffusion coefficient for species i in air, D_p (m) is the particle
306 diameter, $f(Kn, \alpha)$ is a correction term to account for non-continuum mass transfer depending on
307 Knudsen number (Kn) and mass accommodation coefficient (α), f_i is the mole fraction of species
308 i , $C_i^*(T)$ is the saturation concentration at temperature (T) of the heater tube, M_i (kg mol^{-1}) is the
309 molecular weight of species i , ρ_i (kg m^{-3}) is its density and $N_p(D_p)$ (cm^{-3}) is the number
310 concentration of particles with a diameter D_p .

311 The correction term $f(Kn, \alpha)$ is determined by the following equation (Seinfeld and Pandis,
312 2016):

$$313 \quad f(Kn, \alpha) = \frac{1+Kn}{1+2Kn(1+Kn)/\alpha}$$
$$314 \quad Kn = \frac{2\lambda_i}{D_p} \quad (14)$$

315 where λ_i is the mean free path of species i in the air, which is defined as $\lambda_i = \frac{2D_i}{c_i}$. The c_i is the mean
316 speed of species i and $c_i = \sqrt{\frac{8RT}{\pi M_i}}$.

317 The temperature-dependent $C_i^*(T)$ is estimated from the Clausius-Clapeyron equation:

$$318 \quad C_i^*(T) = C_i^*(T_{ref}) \exp \left[\frac{\Delta H_{vap,i}}{R} \left(\frac{1}{T_{ref}} - \frac{1}{T} \right) \right] \frac{T_{ref}}{T} \quad (15)$$

319 where $\Delta H_{vap,i}$ (kJ mol^{-1}) is the enthalpy of vaporization. The known mass fractions of NH_4NO_3 ,
320 $(\text{NH}_4)_2\text{SO}_4$, and BC were calculated respectively, based on the SP-AMS measurement. The time
321 step of the model was set to be 10^{-3} s. The characteristics of each species were listed in Table 2. The
322 mass fraction of each organic group in different particle sizes was derived by minimizing the squared
323 residuals (SSR) values, $\text{SSR} = \sum_{T_i=T_1}^{T_5} [\text{MFR}_{\text{model}}(T_i, D_p) - \text{MFR}_{\text{measured}}(T_i, D_p)]^2$. The non-
324 linear constrained optimization function “fmincon” in MATLAB (version 2016a, Mathworks Inc.)
325 was used to obtain the optimal fitted result. A constrained of $\sum f_{i,\text{inorganics}} + \sum f_{i,\text{organics}} = 1$ is used.

326 The modeled MFR is strongly dependent on the values of vaporization enthalpy (ΔH_{vap}) and



327 mass accommodation coefficient (α) (Lee et al., 2010; Lee et al., 2011). Thus, a sensitivity test is
328 performed to determine the ΔH_{vap} of OA and α based on the campaign average data (Fig. S4). A
329 linear relationship was adopted between ΔH_{vap} and $\log_{10} C_i^*(T_{ref})$, $\Delta H_{vap} = -a \cdot$
330 $\log_{10} C_i^*(T_{ref}) + b$, where a and b are fitting parameters (Epstein et al., 2010). The a and b values
331 are set to be [0, 4, 8, 12] and [50, 80, 100, 150, 200] in the sensitivity test, respectively, along with
332 $\alpha = [0.01, 0.09, 0.1, 0.5, 0.7, 0.9, 1]$. The results show that the measured MFR was reproduced well
333 (with the lowest SSR of 0.0205, Fig. S5) by using $\Delta H_{vap} = 80 \text{ kJ mol}^{-1}$ with α of 0.09, 0.1 and 0.7,
334 respectively. For simplicity, $\Delta H_{vap} = 80 \text{ kJ mol}^{-1}$ and $\alpha = 0.09$ are considered as the best estimation
335 and adopted in the simulation of the whole campaign datasets. The extracted α value was consistent
336 with the values ($\alpha \leq 0.1$) reported previously (Saha et al., 2015; Park et al., 2013; Saleh et al.,
337 2008; Cappa and Jimenez, 2010), indicating significant resistance to mass transfer during
338 evaporation. In addition, the ΔH_{vap} of OA is of the same magnitude (80-150 kJ mol^{-1}) as reported
339 in the literature (Hong et al., 2017; Saha et al., 2017; Riipinen et al., 2010).

340 Note that the decomposition of particles during the heating process is ignored in the model.
341 Kiyoura and Urano (1970) suggested that ammonium sulfate would decompose to ammonium
342 bisulfate (NH_4HSO_4) or triammonium hydrogen sulfate ($\text{NH}_4)_3\text{H}(\text{SO}_4)_2$, and ammonia (NH_3) when
343 heated to around 160-180 °C. Wang and Hildebrandt Ruiz (2018) also observed thermal
344 decomposition of organics and ammonium sulfate during evaporation by using a Filter Inlet for
345 Gases and AEROSols chemical-ionization mass spectrometer (FIGAERO-CIMS). It suggests that,
346 besides sublimation, decomposition might occur during evaporation of particles. However, the
347 mechanisms of decomposition are complex and remain unclear, which is difficult to simulate in our
348 model. We hence exclude the decomposition of particles from the model for simplicity.



349 3 Results and discussion

350 3.1 Overview

351 Figure 1 shows the temporal profile of PNSD (a), aerosol chemical composition and total mass
352 concentration of $PM_{2.5}$ (b), mass fraction of each component (c), and wind speed and direction (d)
353 during the measurements. Note that the SP-AMS measurement started on 12th October. According
354 to the PNSD data, a total number of 20 new particle formation (NPF) events were observed during
355 the whole campaign. The background particles mainly exhibited unimodal distribution which
356 peaked at a size range of about 80-150 nm. The average particle number concentration (N_{CN}) in the
357 size range of 3-1000 nm was about 12700 cm^{-3} , much lower than that from the rural measurement
358 (18150 cm^{-3}) in 2006 in the PRD region (Rose et al., 2010). A wide accumulation mode was
359 observed during the period prevalent with north wind direction, implying that the air mass from the
360 north could bring pollutants from the city cluster around Guangzhou to the measurement site.

361 The chemical composition and the corresponding mass fraction measured by the SP-AMS (Fig.
362 1 b and c) were consistent with those of PNSD, which showed a significantly high mass
363 concentration of organics when the wind was from the north. The average mass fraction of PM_1 was
364 dominated by organics (51.8%), followed by sulfate (17.5%), nitrate (10.2%), BC (9.9%),
365 ammonium (8.8%), and chloride (1.7%). The mass concentration of organics varied from 3.3 to
366 $123.4\text{ }\mu\text{g m}^{-3}$, with an average value of $20.3\text{ }\mu\text{g m}^{-3}$, lower than the value ($25.7\text{ }\mu\text{g m}^{-3}$) reported in
367 Guangzhou city (Qin et al., 2017), but significantly higher than that was observed ($4.1\text{ }\mu\text{g m}^{-3}$) in
368 Hongkong (Lee et al., 2013). The mass distribution of the chemical species at the Heshan site was
369 similar to that measured in inland China (Chen et al., 2015;Huang et al., 2014), which was



370 dominated by organics from anthropogenic emissions. A distinguished and reproducible diurnal
371 pattern of the mass fraction was observed during the measurement (Fig. 1c), implying that the
372 particle composition was more affected by local emission or photochemical production than other
373 pathways. Organics showed a diurnal pattern with bimodal peaks respectively in the afternoon and
374 evening, which will be discussed later in section 3.3. The temporal profile of GF-PDF (Fig. 2)
375 measured by the H/V-TDMA was consistent with that of chemical composition, which showed a
376 significant diurnal pattern. It suggested that particles at all diameters could be affected by
377 atmospheric chemical processes and local emissions, which will be further discussed in section 3.3.
378 The H/V-TDMA data from 18th to 26th October and 29th October to 3rd November were not available
379 due to instrumental failure. In general, the GF-PDF exhibited a bimodal distribution for particles
380 larger than 30 nm, with a significant more-hygroscopic (MH, $GF > 1.33$) or less-hygroscopic (LH,
381 $1.11 < GF < 1.33$) mode and a less obvious non-hygroscopic (NH, $GF < 1.11$), indicating that these
382 particles were partly externally mixed. The NH mode with primary emissions (e.g., fresh black
383 carbon and some organics) was more obvious in a size range of 50-150 nm than others, suggesting
384 that these particles were more affected by local anthropogenic emissions. The above observation
385 was supported by the size distribution of the BC mass fraction (Fig. S6), which peaked at a size range
386 of about 50-150 nm. Besides, the MH mode shifted to a higher GF value with an increase of particle
387 sizes, implying that larger particles were more aged with a higher fraction of inorganic salt (Fig. S6)
388 and well separated from the freshly emitted counterparts. A similar phenomenal pattern was
389 previously observed in the urban environment, including the PRD region (Hong et al., 2018; Cai et
390 al., 2017; Jiang et al., 2016; Tan et al., 2013b), the North China Plain (Liu et al., 2011; Ma et al., 2016)
391 and other city regions around the world (Yuan et al., 2020; Mochida et al., 2006; Massling et al.,



392 2005).

393 Table 3 summaries the N_{CCN} , activation ratio (AR), D_{50} , and κ_{CCN} values at 0.1%, 0.2%, 0.4%,
394 0.7%, 0.9%, and 1.0% SS during the campaign. The activation ratio is defined as the ratio of N_{CCN}
395 to N_{CN} , that is, $AR = N_{CCN}/N_{CN}$. The average N_{CCN} at 0.1%, 0.2%, 0.4%, 0.7%, 0.9%, and 1.0% SS
396 was about 2507, 4322, 5854, 6834, 7497, and 7862 cm^{-3} , respectively. The N_{CCN} at 0.7% SS was
397 lower than that measured (7900 cm^{-3} at 0.7% SS) in urban Guangzhou (Cai et al., 2018) and at a
398 suburban site (14400 cm^{-3} at 0.864% SS) in the North China Plain (Zhang et al., 2020), but
399 significantly higher than that measured at an urban site (2776 cm^{-3} at 0.68% SS) in São Paulo, Brazil
400 (Almeida et al., 2014). The average AR at the above six SS was 0.20, 0.34, 0.45, 0.52, 0.57, and
401 0.60, respectively. The AR at 0.7% SS was lower than the measured value (0.64 at 0.7% SS) in the
402 urban Guangzhou (Cai et al., 2018), while the corresponding D_{50} (52.56 nm) was lower than that
403 (58.45 nm) in the Guangzhou campaign, implying a higher CCN activity at this site. Thus, the lower
404 AR in this autumn campaign suggested that particles were more centered at smaller sizes, which
405 might be attributed to frequently occurred NPF at the Heshan site. The hygroscopicity parameter κ
406 obtained by the CCNc method were 0.48, 0.47, 0.31, 0.22, 0.20, and 0.20 at the above SS,
407 respectively, which was much higher than those measured by the HTDMA in this study. The
408 average κ values obtained using HTDMA fall in a range of 0.1-0.17 at 30-200 nm (Fig. S7), which
409 were possibly attributed to high fraction of organic matter (Fig. S6). This significant discrepancy
410 between the measured κ_{CCN} and κ_{HTDMA} values is likely attributed to the surfactant effect. It was
411 reported that organics matter in the particles could serve as surfactant and lower surface tension by
412 about 0.01-0.032 N m^{-1} , leading to a higher CCN activity and thus a higher κ_{CCN} (Petters and
413 Kreidenweis, 2013;Ovadnevaite et al., 2017;Liu et al., 2018). According to Eqs. (4) and (5), the



414 κ_{CCN} was more susceptible affected by the value of surface tension than that of κ_{HTDMA} , which would
415 lead to the discrepancy between κ_{CCN} and κ_{HTDMA} values. Note that surface tension effect is not the
416 only factor which leads to a higher κ_{CCN} . It was found that κ_{CCN} could be higher than κ_{HTDMA} , since
417 the existence of the slightly soluble compounds inhibits water uptake under subsaturation conditions
418 (Zhao et al., 2016;Pajunoja et al., 2015;Dusek et al., 2011;Petters et al., 2009).

419 **3.2 The average size-resolved hygroscopicity and volatility of OA**

420 The composition of organics could vary on a large scale with diameters due to different sources
421 and aging processes, which would further affect their properties. Figure 3 presents the average size-
422 resolved hygroscopicity and volatility of OA. The κ_{OA} values (vertical red lines in Fig. 3) ranged
423 from 0.058 to 0.09, within the range (0.05-0.15 at 100 nm) previously reported in the PRD region
424 (Hong et al., 2018) and slightly higher than that (0.03-0.06 at 250 nm) at a mountain site in Germany
425 (Wu et al., 2013). In general, the κ_{OA} values increased with particle sizes from 0.058 at 30 nm to
426 0.09 at 150 and 200 nm, similar to the feature observed in urban and forest environments (Kim et
427 al., 2020;Deng et al., 2019). The increases of the κ_{OA} values with particle sizes could be explained
428 by the oxidation level of organic aerosols (Massoli et al., 2010;Lambe et al., 2011;Xu et al., 2021).
429 Specifically, the hygroscopicity of OA was often found to be positively correlated to its oxidation
430 level (Mei et al., 2013;Lambe et al., 2011), which was usually represented by f_{44} , O/C ratio, or \overline{OS}_c .
431 Thus, the higher κ_{OA} values at larger particle diameters in this study might correspond to a higher
432 aging degree of these particles, and this was confirmed by the increasing trend of f_{44} with particle
433 diameters, i.e., the increasing fraction of CO_2^+ in OA in large particles (Fig. S8). Previous field
434 studies also indicated that f_{44} increased with particle diameters (Kim et al., 2020;Cai et al., 2018),



435 leading to a higher κ_{OA} value.

436 Besides the hygroscopicity of OA, we observed the size dependence of volatility. As shown in
437 Fig. 3, the mass fraction of ELVOA increases from 0.16 to 0.30 with the particle diameter, indicating
438 that the particles could be more aged at larger diameters, consistent with the higher κ_{OA} values as
439 discussed above. The ELVOA fraction in this campaign was higher than that in Beijing in summer
440 (0.13) measured by a thermodenuder (TD) coupled to an AMS (Xu et al., 2019), but similar to that
441 in Athens (0.3) using a similar TD system (Louvaris et al., 2017). The SVOA generally contributed
442 42%-57% to the OA at all measured sizes, comparable to the values reported in Centreville and
443 Raleigh (66-75%, Saha et al., 2017), Beijing (64%, Xu et al., 2019) and Mexico City (39%-73%,
444 Cappa and Jimenez, 2010). Note that the relationship between volatility and oxidation state of OA
445 is not usually strong. Saha et al. (2017) reported weak correlations ($R < 0.3$) between the mean
446 volatility ($\overline{C^*}$) and the mean oxidation state ($\overline{\text{OS}}_C$). Hong et al. (2017) also found that the volatility
447 distribution of OA derived from the combined V-TDMA and evaporation dynamic model could not
448 be fully explained by the organic fractions determined by the PMF analysis based on the AMS data.
449 This is probably because the volatility was not only dependent on the $\overline{\text{OS}}_C$, but also the number of
450 atomic carbon (Donahue et al., 2011). In spite of this, the size-resolved volatility distribution can
451 provide a rough estimate of the aging degree of OA.

452 3.3 The diurnal variation of OA hygroscopicity and volatility

453 As discussed in Sect. 3.2, the hygroscopicity and volatility of OA could vary on a large range
454 with particle diameters, which might be attributed to photochemical reactions and the OA sources.
455 In this section, the diurnal variation of hygroscopicity and volatility of OA at different particle sizes



456 was investigated, in combination with the PMF results. In general, the mass fraction of organics
457 showed an obvious diurnal pattern during the whole campaign, with two peaks at about 14:00 and
458 19:00 LT (Fig. 4a), implying significant impacts of photochemical reactions and local emissions.
459 Based on the PMF results (Fig. 5), the afternoon peak was attributed to secondary organics aerosol
460 (SOA) formation (aBBOA and LOOA) during daytime, while the evening peak was explained by
461 local residential activity (e.g., biomass burning and cooking, HOA and BBOA), as will be discussed
462 later. A similar late-afternoon peak was observed in Hong Kong (Lee et al., 2013), where the OA
463 enhancement was mainly contributed by traffic emissions. The f_{44} remained at a high level during
464 daytime, consistent with strong photochemical reactions. A similar diurnal pattern was observed in
465 the urban and sub-urban regions (Hong et al., 2018; Hu et al., 2016; Thalman et al., 2017), suggesting
466 the consistent aging processes of pre-existing OA. In contrast, Deng et al. (2019) reported a relative
467 low OA oxidation state during daytime in a forest environment, which could be explained by the
468 SOA formation through photochemical oxidation of BVOCs.

469 The calculated κ_{HTDMA} and κ_{AMS} (the blue and red lines in Fig. 4b, respectively) values at 200
470 nm based on Eqs. (4) and (7) both reached minimum during daytime which was consistent with high
471 OA fractions. This may be explained by lower hygroscopic of OA than inorganics as found in
472 previous studies (Pajunoja et al., 2015; Zhao et al., 2015; Kuang et al., 2020b) as well as the low κ_i
473 values shown in Table 1. Although OA in a higher oxidation state could be hydrophilic (Massoli et
474 al., 2010), the primary OA is usually considered to be hydrophobic substance and their mixture
475 would be less hygroscopic (usually with average $\kappa = 0.1$). The κ_{AMS} values were generally consistent
476 with those of the κ_{HTDMA} during daytime while the overestimated κ_{OA} was observed during nighttime.
477 This implies a lower κ_{OA} value than 0.1 at 200 nm during the nighttime, probably due to less



478 oxidation processes at night than those under the sunlight.

479 The average diurnal profile of PNSD is shown in Fig. 4c. Besides a stable accumulation mode
480 peaked at around 100 nm, a significantly growing mode of particle number from 20nm to 80 nm
481 was observed from 12:00 to 20:00 LT, which could be attributed to the frequently occurred NPF
482 during the campaign (Fig. 1a).

483 The size-resolved diurnal variations of κ_{OA} was explored in Fig. 6. Note that the κ_{OA} values are
484 presented in 2-hour resolution due to the low data coverage (Figs. 1 and 2). In general, a significantly
485 different pattern was observed between Aitken mode and accumulation mode. For Aitken mode
486 particles (30-100 nm), the κ_{OA} values were higher (0.05-0.1) before dawn than those (0.02-0.07)
487 during daytime, while this trend began to overturn at 150 and 200 nm, where the κ_{OA} values peaked
488 at noon (~ 0.09 , Fig. 6). As reported in literature, the hygroscopicity of organics was partly dependent
489 on the aging degree (Liu et al., 2021; Zhao et al., 2016; Kim et al., 2020). The diurnal characteristics
490 of the size-resolved κ_{OA} indicate that the OA in small particles (30-100 nm) was fresh and became
491 aged in large particles. For the same campaign, Kuang et al. (2021) showed a negative correlation
492 ($R=-0.25$) between LOOA and κ_{OA} , while a positive correlation ($R=0.35$) between aBBOA and κ_{OA} .
493 Thus, the decrease of κ_{OA} for Aitken mode particles during daytime might be attributed to the
494 daytime formation of LOOA through gas-particle partitioning (Fig. 5). A similar phenomenon was
495 reported by Deng et al. (2019) in a forest environment, which might be attributed to the
496 photochemical reactions of BVOCs. Therefore, OA in small particles might be less aged and was
497 primarily contributed by photochemical oxidation of VOCs. In contrast, it is likely that the
498 accumulation mode particles became aged through photochemical oxidation during daylight, as
499 evidenced by higher fractions of ELVOA at 200 nm and higher κ_{OA} (Figs. 6 and 7) during daytime.



500 According to the PMF analysis, the daytime formation of aBBOA likely resulted from the aging
501 processes of primary OA or biomass burning related precursors (Fig. 5). As suggested by Kuang et
502 al. (2021), the daytime formation of aBBOA (Fig. 5) would lead to an increase of κ_{OA} , which likely
503 explained the noontime κ_{OA} peak at 150 and 200 nm. It suggested that the OA in the accumulation
504 mode was more influenced by the aging processes through photochemical reactions (leading to
505 aBBOA formation).

506 The average size-resolved volatility distribution of OA during daytime (8:00 to 16:00 LT) and
507 nighttime (20:00 to 4:00 LT) was demonstrated in Fig. 7. A higher fraction of semi-volatile organic
508 aerosol (SVOA) was observed at six measured sizes (30, 50, 80, 100, 150, and 200 nm) during
509 daytime. SVOA was usually related to primary emission (e.g., traffic, biomass burning) and gas-
510 particle partitioning (Donahue et al., 2012; Jathar et al., 2020; Hong et al., 2017; Saha et al., 2017).
511 Two primary emission factors, BBOA and HOA, remained at a relative low level during daytime,
512 suggesting that the higher fraction of SVOA during daylight might be more originated from gas-
513 particle partitioning. Note that gas-particle partitioning (leading to LOOA formation) could occur
514 at all measured diameters, as shown by the higher daytime fractions of SVOA (Fig. 7). In summary,
515 the above results indicate that the negative effect of LOOA on κ_{OA} might exist at all diameters, while
516 the positive effect of aBBOA was more dominant at larger particle sizes.

517 Meanwhile, the decreasing trend of κ_{OA} was observed from 18:00 to 24:00 at 80 and 100 nm
518 which might be related to the high mass fraction of OA from primary emissions (HOA and BBOA,
519 Fig. 5), owing to their hydrophobic nature. These two primary factors were associated with traffic
520 emissions, cooking and biomass burning. Zhang et al. (2005b) constructed the size distribution of
521 HOA based on the size-resolved m/z 44 and 57 from the AMS measurement and showed that HOA



522 was dominant (~75%) in ultrafine particles ($D_{va} < 100$ nm). The size-resolved PMF results from Sun
523 et al. (2012) also indicated a high mass fraction of HOA (0.3-0.4) in Aitken mode particles. The
524 mass distribution of BC could be used to represent the distribution of primary OA (Cubison et al.,
525 2008; Wang et al., 2010; Zhang et al., 2005a) due to similar source origins for BC and HOA/BBOA.
526 The average mass fraction of BC peaked at about 80-100 nm (Fig. S6a), suggesting that HOA and
527 BBOA might be dominant at this size range. The BC peaks at 80 nm and 100 nm were consistent
528 with those of the SVOA mass fraction (Fig. 3), which was attributed to biomass burning as similar
529 characteristics for the BC peak were shown in other studies (May et al., 2013; Huffman et al.,
530 2009; Donahue et al., 2011). Furthermore, this conclusion was supported by the hygroscopicity
531 measurements as a significant NH mode for 80-100 nm particles was found (Fig. 2). Overall, these
532 results highlight that the diurnal variation of physicochemical properties of OA could vary in a large
533 range with particle diameters, and further investigation is needed.

534 **3.4 Implication for CCN activity**

535 The CCN activity and its prediction is essential in global climate model and evaluation. A κ_{OA}
536 value of 0.1~0.15 was widely adopted in the prediction of N_{CCN} based on aerosol chemical
537 composition (Meng et al., 2014; Wang et al., 2010; Almeida et al., 2014). As discussed in Sect. 3.3,
538 the κ_{OA} values might be dependent on particle sizes and vary diurnally, which in turn affect N_{CCN} .
539 Here, different κ_{OA} values were adopted to predict N_{CCN} and the impact of κ_{OA} on N_{CCN} was
540 investigated through comparison between the predicted and measured N_{CCN} . Note that we only
541 discussed the N_{CCN} at 0.1%, 0.2%, 0.4% and 0.7% SS, since the D_{50} at higher SS (0.9% and 1.0%)
542 was within a narrow range (35-60 nm).



543 The N_{CCN} at a certain SS can be calculated using PNSD and D_{50} :

$$544 N_{CCN,p}(SS) = \int_{D_{50}}^{\infty} n_i d \log D p_i \quad (16)$$

545 where n_i is the particle distribution function at $D p_i$ and D_{50} is determined from the κ_{AMS} using Eqs.

546 (5) and (7). The D_{50} at 0.1%, 0.2%, 0.4% and 0.7% SS ranged from about 130-160 nm, 90-110 nm,

547 60-80 nm and 45-60 nm, respectively. Three κ_{OA} schemes were proposed to predict N_{CCN} : (1) fixed

548 κ_{OA} , where κ_{OA} was assumed to be 0.1 for all size particles. (2) size-resolved κ_{OA} (SR κ_{OA}), where

549 κ_{OA} was taken from average size-resolved κ_{OA} (κ_{OA} at 50, 80, 100 and 150 nm for 0.7%, 0.4%, 0.2%

550 and 0.1% SS, respectively) in Sect. 3.2. (3) size-resolved diurnal κ_{OA} (SR diurnal κ_{OA}), where κ_{OA}

551 was the average diurnal value of κ_{OA} at each diameter (κ_{OA} at 50, 80, 100 and 150 nm for 0.7%,

552 0.4%, 0.2% and 0.1% SS, respectively) as shown in Sect. 3.3. The κ_{AMS} was calculated based on the

553 chemical composition at the corresponding D_{50} range. Note that the N_{CCN} prediction based on the

554 SR diurnal κ_{OA} scheme was presented in 2 h time resolution and the particles were assumed to be

555 internally mixed in Eq. (16). Cai et al. (2018) compared different approaches in predicting N_{CCN} and

556 found that mixing state assumption played a minor role in the prediction, while the surfactant effect

557 should be taken into account. As aforementioned, organics can increase the CCN activity by

558 decreasing surface tension, which might lead to significant discrepancy between κ_{HTDMA} and κ_{CCN}

559 in this campaign (Fig. S7). In addition, this effect could result in a significant underestimation of

560 N_{CCN} (Ovadnevaite et al., 2017; Liu et al., 2018; Good et al., 2010; Noziere, 2016).

561 Here, we evaluate the surface tension effect by comparing κ_{HTDMA} and κ_{CCN} as a function of

562 $\sigma_{s/a}$ (Fig. S9). The κ_{CCN} reached κ_{HTDMA} when the $\sigma_{s/a}$ values were set to be about 0.059 N m⁻¹ at

563 0.7%, 0.9% and 1.0% SS, 0.053 N m⁻¹ at 0.4% SS, 0.047 N m⁻¹ at 0.2% SS, and 0.049 N m⁻¹ at 0.1%

564 SS, respectively. Thus, we adopted $\sigma_{s/a}$ values of 0.049, 0.047, 0.053 and 0.059 N m⁻¹ to predict



565 N_{CCN} at 0.1%, 0.2%, 0.4% and 0.7% SS, respectively. In general, the N_{CCN} prediction could be
566 significantly improved by considering the surfactant effect (Fig. S10).

567 The deviation of the N_{CCN} prediction ($\delta_{N_{CCN}}$) at a certain SS is defined as (Cai et al., 2021b):

$$568 \delta_{N_{CCN}}(SS) = \frac{N_{CCN,m}(SS) - N_{CCN,p}(SS)}{N_{CCN,m}(SS)} 100\% \quad (17)$$

569 where $N_{CCN,m}(SS)$ is the measured N_{CCN} at a specific SS. A negative $\delta_{N_{CCN}}$ indicates an
570 overestimate of N_{CCN} , and vice versa.

571 Figure 8 shows the $\delta_{N_{CCN}}$ at different SS for the three κ_{OA} schemes. Fixed κ_{OA} scheme gave
572 generally a negative value of $\delta_{N_{CCN}}$ (-0.18 to -0.02) at 0.7% SS, indicating an N_{CCN} overestimation,
573 due to lower κ_{OA} values for smaller particles. A significant diurnal pattern of $\delta_{N_{CCN}}$ was observed at
574 all SS. The $\delta_{N_{CCN}}$ was relatively higher during daytime at 0.1% SS, while an opposite pattern was
575 shown at high SS, consistent with the size-dependent variation of κ_{OA} (Fig. 6). Hence, the fixed κ_{OA}
576 scheme could lead to an obvious discrepancy in the N_{CCN} prediction as SS increased. The results
577 based on the SR κ_{OA} scheme showed that the minimum $\delta_{N_{CCN}}$ value at 0.7% SS increased from -
578 0.18 in the fixed κ_{OA} scheme to -0.08, indicating the improvement for the N_{CCN} prediction at high
579 SS (Fig. 8b). However, only minor improvement was observed at SS lower than 0.4 % because of
580 the low employed κ_{OA} (about 0.08), which was close to the κ_{OA} value (0.1) adopted in the fixed κ_{OA}
581 scheme. A significant difference of $\delta_{N_{CCN}}$ was still observed in the diurnal pattern at high and low
582 SS, implying the impact of the diurnal variation of κ_{OA} on the N_{CCN} prediction. To further investigate
583 this impact, the SR diurnal κ_{OA} scheme was employed to calculate $\delta_{N_{CCN}}$ and the results were shown
584 in Fig. 8c. The $\delta_{N_{CCN}}$ value at 0.7% SS varied from -0.04 to 0.09 with an average value of 0, whereas
585 it ranged from 0 to 0.11 at 0.1% SS. Hence, the discrepancies of $\delta_{N_{CCN}}$ among different SS became
586 minor compared to the other two schemes as a relatively flat diurnal pattern of $\delta_{N_{CCN}}$ was observed



587 at all SS. It implies that better prediction of N_{CCN} could be achieved by considering the diurnal
588 variation and the size dependence of κ_{OA} .

589 4. Conclusions

590 A rural field measurement was conducted at the Heshan supersite in the PRD region of China
591 during October and November 2019. We investigated the diurnal variation and size dependence in
592 the hygroscopicity and volatility of OA in combination with the PMF analysis of the AMS data. The
593 impacts of OA on the CCN number concentration at different SS were discussed for various given
594 size-dependent κ_{OA} values.

595 In general, the average κ_{OA} values varied from 0.058 at 30 nm to 0.09 at 200 nm, indicating a
596 higher oxidation degree of OA at larger sizes than at smaller sizes. This is consistent with particle
597 volatility: the mass fraction of ELVOA increased (0.16-0.30) with increasing particle diameters.

598 Our results suggest that the formation and aging processes of OA might vary with particle sizes.
599 An oppositely diurnal pattern of κ_{OA} was observed between Aitken mode (30-100 nm) and
600 Accumulation mode (150 and 200 nm) particles, suggesting different atmospheric evolution
601 processes of OA at different diameters. The gas-particle partitioning could decrease the κ_{OA} , while
602 the aging processes of preexisting particles could enhance the hygroscopicity of OA. The κ_{OA} values
603 for 30-100 nm particles reached minimal (0.02-0.07) and a high κ_{OA} value (\sim 0.09) for 150 and 200
604 nm particles was observed during daytime, suggesting that the aging processes of preexisting
605 particles were more dominant at accumulation mode particles. In addition, the mass fraction of
606 SVOA was higher during daytime at all measured diameters, implying that the formation of LOOA



607 through gas-particle partitioning was independent of particle diameters.

608 The impact of the size-resolved diurnal variation of κ_{OA} on the N_{CCN} was investigated. The use
609 of fixed κ_{OA} ($\kappa_{\text{OA}}=0.1$) overestimated the N_{CCN} up to 18% at 0.7% SS. The diurnal deviation became
610 obvious at 0.7% SS and minor at 0.1% SS during daytime, owing to the size-dependent variation of
611 κ_{OA} . The N_{CCN} prediction at 0.7% SS was improved if the SR κ_{OA} scheme was used, while the
612 diurnal variation of $\delta_{N_{\text{CCN}}}$ still existed. Better predictions can be obtained by using SR diurnal κ_{OA} .
613 Our results highlight that the physical properties of OA can vary in a large range at different size
614 ranges due to the formation and aging processes, and the size-resolved diurnal variation in κ_{OA} plays
615 an important role in the N_{CCN} prediction at different SS. Further studies on the size-resolved
616 physicochemical properties of OA should be performed in different environments to better
617 understand their impact on cloud formation and hence climate.

618

619 *Data availability.* Data from the measurements are available at
620 <https://doi.org/10.6084/m9.figshare.18094277.v1> (Cai et al., 2022).

621

622 *Supplement.* The supplement related to this article is available online at xxx.

623

624 *Author contributions.* MC, SH, BY and LL designed the research. MC, SH, MS, BY, YP, ZW, DC,
625 WC, QS, WL, BL and QS performed the measurements. MC, SH, BL, QS, LL, BY, WH, WC,
626 QS, WL, YP, ZW, HT, HX, FL, DX, TD, JS and JZ analyzed the data. MC, SH and LL wrote the
627 paper with contributions from all co-authors.

628



629 *Competing interests.* The authors declare that they have no conflict of interest.

630

631 *Financial support.* This work was supported by the Key-Area Research and Development Program
632 of Guangdong Province (grant no. 2019B110206001), the National Key R&D Plan of China (grant
633 no. 2019YFE0106300 and 2018YFC0213904), the National Natural Science Foundation of China
634 (grant nos. 41877302, 91644225, 41775117 and 41807302), Guangdong Natural Science Funds for
635 Distinguished Young Scholar (grant no. 2018B030306037), Guangdong Innovative and
636 Entrepreneurial Research Team Program (grant no. 2016ZT06N263), Guangdong Province Key
637 Laboratory for Climate Change and Natural Disaster Studies (grant no. 2020B1212060025),
638 Guangdong Basic and Applied Basic Research Foundation (grant nos. 2019A1515110790 and
639 2019A1515110791), Science and Technology Research project of Guangdong Meteorological
640 Bureau (grant no. GRMC2018M07), the Natural Science Foundation of Guangdong Province,
641 China (grant no. 2016A030311007), Science and Technology Innovation Team Plan of Guangdong
642 Meteorological Bureau (grant no. GRMCTD202003), and Science and Technology Program of
643 Guangdong Province (Science and Technology Innovation Platform Category, No.
644 2019B121201002).

645

646 *Acknowledgements.* Additional support from the crew of the Heshan supersite and Guangdong
647 Environmental Monitoring Center is greatly acknowledged.

648



649 **References**

650 Almeida, G. P., Brito, J., Morales, C. A., Andrade, M. F., and Artaxo, P.: Measured and
651 modelled cloud condensation nuclei (CCN) concentration in São Paulo, Brazil: the importance of
652 aerosol size-resolved chemical composition on CCN concentration prediction, *Atmos. Chem. Phys.*,
653 14, 7559-7572, 10.5194/acp-14-7559-2014, 2014.

654 Cai, J., Chu, B., Yao, L., Yan, C., Heikkinen, L. M., Zheng, F., Li, C., Fan, X., Zhang, S., Yang,
655 D., Wang, Y., Kokkonen, T. V., Chan, T., Zhou, Y., Dada, L., Liu, Y., He, H., Paasonen, P., Kujansuu,
656 J. T., Petäjä, T., Mohr, C., Kangasluoma, J., Bianchi, F., Sun, Y., Croteau, P. L., Worsnop, D. R.,
657 Kerminen, V. M., Du, W., Kulmala, M., and Daellenbach, K. R.: Size-segregated particle number
658 and mass concentrations from different emission sources in urban Beijing, *Atmos. Chem. Phys.*, 20,
659 12721-12740, 10.5194/acp-20-12721-2020, 2020.

660 Cai, M., Huang, S., Li, L., Yuan, B., Shao, M., and Zhao, J.: Distinct size dependence and
661 diurnal variation of OA hygroscopicity, volatility, and CCN activity at a rural site in the Pearl River
662 Delta (PRD) region, China. figshare. Dataset., <https://doi.org/10.6084/m9.figshare.18094277.v1>,
663 2022.

664 Cai, M., Tan, H., Chan, C. K., Mochida, M., Hatakeyama, S., Kondo, Y., Schurman, M. I., Xu,
665 H., Li, F., and Shimada, K.: Comparison of Aerosol Hygroscopicity, Volatility, and Chemical
666 Composition between a Suburban Site in the Pearl River Delta Region and a Marine Site in Okinawa,
667 *Aerosol Air Qual. Res.*, 2017.

668 Cai, M., Tan, H., Chan, C. K., Qin, Y., Xu, H., Li, F., Schurman, M. I., Liu, L., and Zhao, J.:
669 The size-resolved cloud condensation nuclei (CCN) activity and its prediction based on aerosol
670 hygroscopicity and composition in the Pearl Delta River (PRD) region during wintertime 2014,
671 *Atmos. Chem. Phys.*, 18, 16419-16437, 2018.

672 Cai, M., Liang, B., Sun, Q., Liu, L., Yuan, B., Shao, M., Huang, S., Peng, Y., Wang, Z., Tan,
673 H., Li, F., Xu, H., Chen, D., and Zhao, J.: The important roles of surface tension and growth rate in
674 the contribution of new particle formation (NPF) to cloud condensation nuclei (CCN) number
675 concentration: evidence from field measurements in southern China, *Atmos. Chem. Phys.*, 21, 8575-
676 8592, 10.5194/acp-21-8575-2021, 2021a.



677 Cai, M. F., Liang, B. L., Sun, Q. B., Zhou, S. Z., Yuan, B., Shao, M., Tan, H. B., Xu, Y. S., Ren,
678 L. H., and Zhao, J.: Contribution of New Particle Formation to Cloud Condensation Nuclei Activity
679 and its Controlling Factors in a Mountain Region of Inland China, *J. Geophys. Res. Atmos.*, 126,
680 e2020JD034302, <https://doi.org/10.1029/2020JD034302>, 2021b.

681 Canagaratna, M. R., Jayne, J. T., Jimenez, J. L., Allan, J. D., Alfarra, M. R., Zhang, Q., Onasch,
682 T. B., Drewnick, F., Coe, H., Middlebrook, A., Delia, A., Williams, L. R., Trimborn, A. M.,
683 Northway, M. J., DeCarlo, P. F., Kolb, C. E., Davidovits, P., and Worsnop, D. R.: Chemical and
684 microphysical characterization of ambient aerosols with the aerodyne aerosol mass spectrometer,
685 *Mass Spectrom. Rev.*, 26, 185-222, [10.1002/mas.20115](https://doi.org/10.1002/mas.20115), 2007.

686 Cappa, C. D., and Jimenez, J. L.: Quantitative estimates of the volatility of ambient organic
687 aerosol, *Atmos. Chem. Phys.*, 10, 5409-5424, [10.5194/acp-10-5409-2010](https://doi.org/10.5194/acp-10-5409-2010), 2010.

688 Chang, R. Y. W., Slowik, J. G., Shantz, N. C., Vlasenko, A., Liggio, J., Sjostedt, S. J., Leaitch,
689 W. R., and Abbatt, J. P. D.: The hygroscopicity parameter (κ) of ambient organic aerosol at a field
690 site subject to biogenic and anthropogenic influences: relationship to degree of aerosol oxidation,
691 *Atmos. Chem. Phys.*, 10, 5047-5064, [10.5194/acp-10-5047-2010](https://doi.org/10.5194/acp-10-5047-2010), 2010.

692 Chen, C., Sun, Y. L., Xu, W. Q., Du, W., Zhou, L. B., Han, T. T., Wang, Q. Q., Fu, P. Q., Wang,
693 Z. F., Gao, Z. Q., Zhang, Q., and Worsnop, D. R.: Characteristics and sources of submicron aerosols
694 above the urban canopy (260 m) in Beijing, China, during the 2014 APEC summit, *Atmos. Chem.
695 Phys.*, 15, 12879-12895, [10.5194/acp-15-12879-2015](https://doi.org/10.5194/acp-15-12879-2015), 2015.

696 Chen, J., Budisulistiorini, S. H., Itoh, M., Lee, W. C., Miyakawa, T., Komazaki, Y., Yang, L. D.
697 Q., and Kuwata, M.: Water uptake by fresh Indonesian peat burning particles is limited by water-
698 soluble organic matter, *Atmos. Chem. Phys.*, 17, 11591-11604, [10.5194/acp-17-11591-2017](https://doi.org/10.5194/acp-17-11591-2017), 2017.

699 Cheung, H. H., Tan, H., Xu, H., Li, F., Wu, C., Yu, J. Z., and Chan, C. K.: Measurements of
700 non-volatile aerosols with a VTDMA and their correlations with carbonaceous aerosols in
701 Guangzhou, China, *Atmos. Chem. Phys.*, 16, 8431-8446, 2016.

702 Cubison, M. J., Ervens, B., Feingold, G., Docherty, K. S., Ulbrich, I. M., Shields, L., Prather,
703 K., Hering, S., and Jimenez, J. L.: The influence of chemical composition and mixing state of Los
704 Angeles urban aerosol on CCN number and cloud properties, *Atmos. Chem. Phys.*, 8, 5649-5667,
705 [10.5194/acp-8-5649-2008](https://doi.org/10.5194/acp-8-5649-2008), 2008.



706 Deng, Y., Kagami, S., Ogawa, S., Kawana, K., Nakayama, T., Kubodera, R., Adachi, K.,
707 Hussein, T., Miyazaki, Y., and Mochida, M.: Hygroscopicity of Organic Aerosols and Their
708 Contributions to CCN Concentrations Over a Midlatitude Forest in Japan, *J. Geophys. Res. Atmos.*,
709 123, 9703-9723, 10.1029/2017JD027292, 2018.

710 Deng, Y., Yai, H., Fujinari, H., Kawana, K., Nakayama, T., and Mochida, M.: Diurnal variation
711 and size dependence of the hygroscopicity of organic aerosol at a forest site in Wakayama, Japan:
712 their relationship to CCN concentrations, *Atmos. Chem. Phys.*, 19, 5889-5903, 10.5194/acp-19-
713 5889-2019, 2019.

714 Donahue, N. M., Epstein, S. A., Pandis, S. N., and Robinson, A. L.: A two-dimensional
715 volatility basis set: 1. organic-aerosol mixing thermodynamics, *Atmos. Chem. Phys.*, 11, 3303-3318,
716 10.5194/acp-11-3303-2011, 2011.

717 Donahue, N. M., Kroll, J. H., Pandis, S. N., and Robinson, A. L.: A two-dimensional volatility
718 basis set – Part 2: Diagnostics of organic-aerosol evolution, *Atmos. Chem. Phys.*, 12, 615-634,
719 10.5194/acp-12-615-2012, 2012.

720 Dusek, U., Frank, G. P., Massling, A., Zeromskiene, K., Iinuma, Y., Schmid, O., Helas, G.,
721 Hennig, T., Wiedensohler, A., and Andreae, M. O.: Water uptake by biomass burning aerosol at sub-
722 and supersaturated conditions: closure studies and implications for the role of organics, *Atmos.*
723 *Chem. Phys.*, 11, 9519-9532, 10.5194/acp-11-9519-2011, 2011.

724 Engelhart, G. J., Moore, R. H., Nenes, A., and Pandis, S. N.: Cloud condensation nuclei activity
725 of isoprene secondary organic aerosol, *J. Geophys. Res. Atmos.*, 116,
726 <https://doi.org/10.1029/2010JD014706>, 2011.

727 Epstein, S. A., Riipinen, I., and Donahue, N. M.: A Semiempirical Correlation between
728 Enthalpy of Vaporization and Saturation Concentration for Organic Aerosol, *Environ. Sci. Technol.*,
729 44, 743-748, 10.1021/es902497z, 2010.

730 Gantt, B., and Meskhidze, N.: The physical and chemical characteristics of marine primary
731 organic aerosol: a review, *Atmos. Chem. Phys.*, 13, 3979-3996, 10.5194/acp-13-3979-2013, 2013.

732 Good, N., Topping, D., Allan, J., Flynn, M., Fuentes, E., Irwin, M., Williams, P., Coe, H., and
733 McFiggans, G.: Consistency between parameterisations of aerosol hygroscopicity and CCN activity
734 during the RHaMBLe discovery cruise, *Atmos. Chem. Phys.*, 10, 3189-3203, 2010.



735 Guo, J., Zhou, S., Cai, M., Zhao, J., Song, W., Zhao, W., Hu, W., Sun, Y., He, Y., Yang, C., Xu,
736 X., Zhang, Z., Cheng, P., Fan, Q., Hang, J., Fan, S., Wang, X., and Wang, X.: Characterization of
737 submicron particles by time-of-flight aerosol chemical speciation monitor (ToF-ACSM) during
738 wintertime: aerosol composition, sources, and chemical processes in Guangzhou, China, *Atmos.*
739 *Chem. Phys.*, 20, 7595-7615, 10.5194/acp-20-7595-2020, 2020.

740 Gysel, M., Crosier, J., Topping, D. O., Whitehead, J. D., Bower, K. N., Cubison, M. J., Williams,
741 P. I., Flynn, M. J., McFiggans, G. B., and Coe, H.: Closure study between chemical composition
742 and hygroscopic growth of aerosol particles during TORCH2, *Atmos. Chem. Phys.*, 7, 6131-6144,
743 10.5194/acp-7-6131-2007, 2007.

744 Hallquist, M., Wenger, J. C., Baltensperger, U., Rudich, Y., Simpson, D., Claeys, M., Dommen,
745 J., Donahue, N., George, C., and Goldstein, A.: The formation, properties and impact of secondary
746 organic aerosol: current and emerging issues, *Atmospheric chemistry and physics*, 9, 5155-5236,
747 2009.

748 Hong, J., Äijälä, M., Häme, S. A. K., Hao, L., Duplissy, J., Heikkinen, L. M., Nie, W., Mikkilä,
749 J., Kulmala, M., Prisle, N. L., Virtanen, A., Ehn, M., Paasonen, P., Worsnop, D. R., Riipinen, I.,
750 Petäjä, T., and Kerminen, V. M.: Estimates of the organic aerosol volatility in a boreal forest using
751 two independent methods, *Atmos. Chem. Phys.*, 17, 4387-4399, 10.5194/acp-17-4387-2017, 2017.

752 Hong, J., Xu, H., Tan, H., Yin, C., Hao, L., Li, F., Cai, M., Deng, X., Wang, N., Su, H., Cheng,
753 Y., Wang, L., Petäjä, T., and Kerminen, V. M.: Mixing state and particle hygroscopicity of organic-
754 dominated aerosols over the Pearl River Delta region in China, *Atmos. Chem. Phys.*, 18, 14079-
755 14094, 10.5194/acp-18-14079-2018, 2018.

756 Hu, W., Hu, M., Hu, W., Jimenez, J. L., Yuan, B., Chen, W., Wang, M., Wu, Y., Chen, C., Wang,
757 Z., Peng, J., Zeng, L., and Shao, M.: Chemical composition, sources, and aging process of
758 submicron aerosols in Beijing: Contrast between summer and winter, *J. Geophys. Res. Atmos.*, 121,
759 1955-1977, <https://doi.org/10.1002/2015JD024020>, 2016.

760 Huang, R.-J., Zhang, Y., Bozzetti, C., Ho, K.-F., Cao, J.-J., Han, Y., Daellenbach, K. R., Slowik,
761 J. G., Platt, S. M., and Canonaco, F.: High secondary aerosol contribution to particulate pollution
762 during haze events in China, *Nature*, 514, 218, 2014.

763 Huang, S., Wu, Z., Poulain, L., van Pinxteren, M., Merkel, M., Assmann, D., Herrmann, H.,



764 and Wiedensohler, A.: Source apportionment of the organic aerosol over the Atlantic Ocean from
765 53°N to 53°S: significant contributions from marine emissions and long-range transport, *Atmos.*
766 *Chem. Phys.*, 18, 18043-18062, 10.5194/acp-18-18043-2018, 2018.

767 Huffman, J. A., Docherty, K. S., Aiken, A. C., Cubison, M. J., Ulbrich, I. M., DeCarlo, P. F.,
768 Sueper, D., Jayne, J. T., Worsnop, D. R., Ziemann, P. J., and Jimenez, J. L.: Chemically-resolved
769 aerosol volatility measurements from two megacity field studies, *Atmos. Chem. Phys.*, 9, 7161-
770 7182, 10.5194/acp-9-7161-2009, 2009.

771 Jathar, S. H., Sharma, N., Galang, A., Vanderheyden, C., Takhar, M., Chan, A. W. H., Pierce, J.
772 R., and Volckens, J.: Measuring and modeling the primary organic aerosol volatility from a modern
773 non-road diesel engine, *Atmos. Environ.*, 223, 117221,
774 <https://doi.org/10.1016/j.atmosenv.2019.117221>, 2020.

775 Jiang, R., Tan, H., Tang, L., Cai, M., Yin, Y., Li, F., Liu, L., Xu, H., Chan, P. W., and Deng, X.:
776 Comparison of aerosol hygroscopicity and mixing state between winter and summer seasons in Pearl
777 River Delta region, China, *Atmos. Res.*, 169, 160-170, 2016.

778 Jimenez, J. L., Canagaratna, M., Donahue, N., Prevot, A., Zhang, Q., Kroll, J. H., DeCarlo, P.
779 F., Allan, J. D., Coe, H., and Ng, N.: Evolution of organic aerosols in the atmosphere, *Science*, 326,
780 1525-1529, 2009.

781 Kanakidou, M., Seinfeld, J., Pandis, S., Barnes, I., Dentener, F., Facchini, M., Dingenen, R. V.,
782 Ervens, B., Nenes, A., and Nielsen, C.: Organic aerosol and global climate modelling: a review,
783 *Atmos. Chem. Phys.*, 5, 1053-1123, 2005.

784 Kim, N., Yum, S. S., Park, M., Park, J. S., Shin, H. J., and Ahn, J. Y.: Hygroscopicity of urban
785 aerosols and its link to size-resolved chemical composition during spring and summer in Seoul,
786 Korea, *Atmos. Chem. Phys.*, 20, 11245-11262, 10.5194/acp-20-11245-2020, 2020.

787 Kiyoura, R., and Urano, K.: Mechanism, Kinetics, and Equilibrium of Thermal Decomposition
788 of Ammonium Sulfate, *Ind. Eng. Chem. Process Des. Dev.*, 9, 489-494, 10.1021/i260036a001,
789 1970.

790 Kuang, Y., He, Y., Xu, W., Yuan, B., Zhang, G., Ma, Z., Wu, C., Wang, C., Wang, S., Zhang,
791 S., Tao, J., Ma, N., Su, H., Cheng, Y., Shao, M., and Sun, Y.: Photochemical Aqueous-Phase
792 Reactions Induce Rapid Daytime Formation of Oxygenated Organic Aerosol on the North China



- 793 Plain, *Environ. Sci. Technol.*, 54, 3849-3860, 10.1021/acs.est.9b06836, 2020a.
- 794 Kuang, Y., Xu, W., Tao, J., Ma, N., Zhao, C., and Shao, M.: A Review on Laboratory Studies
795 and Field Measurements of Atmospheric Organic Aerosol Hygroscopicity and Its Parameterization
796 Based on Oxidation Levels, *Curr. Pollut. Rep.*, 10.1007/s40726-020-00164-2, 2020b.
- 797 Kuang, Y., Huang, S., Xue, B., Luo, B., Song, Q., Chen, W., Hu, W., Li, W., Zhao, P., Cai, M.,
798 Peng, Y., Qi, J., Li, T., Wang, S., Chen, D., Yue, D., Yuan, B., and Shao, M.: Contrasting effects of
799 secondary organic aerosol formations on organic aerosol hygroscopicity, *Atmos. Chem. Phys.*, 21,
800 10375-10391, 10.5194/acp-21-10375-2021, 2021.
- 801 Lambe, A. T., Onasch, T. B., Massoli, P., Croasdale, D. R., Wright, J. P., Ahern, A. T., Williams,
802 L. R., Worsnop, D. R., Brune, W. H., and Davidovits, P.: Laboratory studies of the chemical
803 composition and cloud condensation nuclei (CCN) activity of secondary organic aerosol (SOA) and
804 oxidized primary organic aerosol (OPOA), *Atmos. Chem. Phys.*, 11, 8913-8928, 10.5194/acp-11-
805 8913-2011, 2011.
- 806 Lee, B.-H., Kostenidou, E., Hildebrandt, L., Riipinen, I., Engelhart, G., Mohr, C., DeCarlo, P.,
807 Mihalopoulos, N., Prevot, A., Baltensperger, U.: Measurement of the ambient organic aerosol
808 volatility distribution: application during the Finokalia Aerosol Measurement Experiment (FAME-
809 2008), *Atmos. Chem. Phys.*, 10, 12149-12160, 2010.
- 810 Lee, B.-H., Pierce, J. R., Engelhart, G. J., and Pandis, S. N.: Volatility of secondary organic
811 aerosol from the ozonolysis of monoterpenes, *Atmos. Environ.*, 45, 2443-2452, 2011.
- 812 Lee, B. P., Li, Y. J., Yu, J. Z., Louie, P. K., and Chan, C. K.: Physical and chemical
813 characterization of ambient aerosol by HR-ToF-AMS at a suburban site in Hong Kong during
814 springtime 2011, *J. Geophys. Res. Atmos.*, 118, 8625-8639, 2013.
- 815 Li, J., Wang, G., Zhou, B., Cheng, C., Cao, J., Shen, Z., and An, Z.: Airborne particulate
816 organics at the summit (2060m, a.s.l.) of Mt. Hua in central China during winter: Implications for
817 biofuel and coal combustion, *Atmos. Res.*, 106, 108-119,
818 <https://doi.org/10.1016/j.atmosres.2011.11.012>, 2012.
- 819 Li, Y. J., Lee, B., Yu, J., Ng, N., and Chan, C. K.: Evaluating the degree of oxygenation of
820 organic aerosol during foggy and hazy days in Hong Kong using high-resolution time-of-flight
821 aerosol mass spectrometry (HR-ToF-AMS), *Atmos. Chem. Phys.*, 13, 8739-8753, 2013.



822 Liu, J., Zhang, F., Xu, W., Sun, Y., Chen, L., Li, S., Ren, J., Hu, B., Wu, H., and Zhang, R.:
823 Hygroscopicity of Organic Aerosols Linked to Formation Mechanisms, *Geophys. Res. Lett.*, 48,
824 e2020GL091683, <https://doi.org/10.1029/2020GL091683>, 2021.

825 Liu, P., Song, M., Zhao, T., Gunthe, S. S., Ham, S., He, Y., Qin, Y. M., Gong, Z., Amorim, J.
826 C., Bertram, A. K., and Martin, S. T.: Resolving the mechanisms of hygroscopic growth and cloud
827 condensation nuclei activity for organic particulate matter, *Nat. Commun.*, 9, 4076,
828 10.1038/s41467-018-06622-2, 2018.

829 Liu, P. F., Zhao, C. S., Göbel, T., Hallbauer, E., Nowak, A., Ran, L., Xu, W. Y., Deng, Z. Z.,
830 Ma, N., Mildenberger, K., Henning, S., Stratmann, F., and Wiedensohler, A.: Hygroscopic properties
831 of aerosol particles at high relative humidity and their diurnal variations in the North China Plain,
832 *Atmos. Chem. Phys.*, 11, 3479-3494, 10.5194/acp-11-3479-2011, 2011.

833 Liu, X., and Wang, J.: How important is organic aerosol hygroscopicity to aerosol indirect
834 forcing?, *Environ. Res. Lett.*, 5, 044010, 10.1088/1748-9326/5/4/044010, 2010.

835 Louvaris, E. E., Florou, K., Karnezi, E., Papanastasiou, D. K., Gkatzelis, G. I., and Pandis, S.
836 N.: Volatility of source apportioned wintertime organic aerosol in the city of Athens, *Atmos.*
837 *Environ.*, 158, 138-147, <https://doi.org/10.1016/j.atmosenv.2017.03.042>, 2017.

838 Noziere, B.: Don't forget the surface, *Science*, 351, 1396-1397, 10.1126/science.aaf3253, 2016.

839 Ma, N., Zhao, C., Tao, J., Wu, Z., Kecorius, S., Wang, Z., Größ, J., Liu, H., Bian, Y., and Kuang,
840 Y.: Variation of CCN activity during new particle formation events in the North China Plain, *Atmos.*
841 *Chem. Phys.*, 16, 8593-8607, 2016.

842 Massling, A., Stock, M., and Wiedensohler, A.: Diurnal, weekly, and seasonal variation of
843 hygroscopic properties of submicrometer urban aerosol particles, *Atmos. Environ.*, 39, 3911-3922,
844 10.1016/j.atmosenv.2005.03.020, 2005.

845 Massoli, P., Lambe, A., Ahern, A., Williams, L., Ehn, M., Mikkilä, J., Canagaratna, M., Brune,
846 W., Onasch, T., and Jayne, J.: Relationship between aerosol oxidation level and hygroscopic
847 properties of laboratory generated secondary organic aerosol (SOA) particles, *Geophys. Res. Lett.*,
848 37, 2010.

849 May, A. A., Levin, E. J. T., Hennigan, C. J., Riipinen, I., Lee, T., Collett Jr., J. L., Jimenez, J.
850 L., Kreidenweis, S. M., and Robinson, A. L.: Gas-particle partitioning of primary organic aerosol



851 emissions: 3. Biomass burning, *J. Geophys. Res. Atmos.*, 118, 11,327-311,338,
852 <https://doi.org/10.1002/jgrd.50828>, 2013.

853 Mei, F., Setyan, A., Zhang, Q., and Wang, J.: CCN activity of organic aerosols observed
854 downwind of urban emissions during CARES, *Atmos. Chem. Phys.*, 13, 12155-12169, 2013.

855 Meng, J. W., Yeung, M. C., Li, Y. J., Lee, B. Y. L., and Chan, C. K.: Size-resolved cloud
856 condensation nuclei (CCN) activity and closure analysis at the HKUST Supersite in Hong Kong,
857 *Atmos. Chem. Phys.*, 14, 10267-10282, [10.5194/acp-14-10267-2014](https://doi.org/10.5194/acp-14-10267-2014), 2014.

858 Mochida, M., Kuwata, M., Miyakawa, T., Takegawa, N., Kawamura, K., and Kondo, Y.:
859 Relationship between hygroscopicity and cloud condensation nuclei activity for urban aerosols in
860 Tokyo, *J. Geophys. Res.*, 111, D23204, [10.1029/2005jd006980](https://doi.org/10.1029/2005jd006980), 2006.

861 Onasch, T. B., Trimborn, A., Fortner, E. C., Jayne, J. T., Kok, G. L., Williams, L. R., Davidovits,
862 P., and Worsnop, D. R.: Soot Particle Aerosol Mass Spectrometer: Development, Validation, and
863 Initial Application, *Aerosol Sci. Tech.*, 46, 804-817, [10.1080/02786826.2012.663948](https://doi.org/10.1080/02786826.2012.663948), 2012.

864 Ovadnevaite, J., Zuend, A., Laaksonen, A., Sanchez, K. J., Roberts, G., Ceburnis, D., Decesari,
865 S., Rinaldi, M., Hodas, N., Facchini, M. C., Seinfeld, J. H., and O' Dowd, C.: Surface tension
866 prevails over solute effect in organic-influenced cloud droplet activation, *Nature*, 546, 637-641,
867 [10.1038/nature22806](https://doi.org/10.1038/nature22806), 2017.

868 Paatero, P., and Tapper, U.: Positive matrix factorization: A non-negative factor model with
869 optimal utilization of error estimates of data values, *Environmetrics*, 5, 111-126,
870 [10.1002/env.3170050203](https://doi.org/10.1002/env.3170050203), 1994.

871 Paatero, P.: Least squares formulation of robust non-negative factor analysis, *Chemometr Intell*
872 *Lab. 37*, 23-35, [10.1016/S0169-7439\(96\)00044-5](https://doi.org/10.1016/S0169-7439(96)00044-5), 1997.

873 Pajunoja, A., Lambe, A. T., Hakala, J., Rastak, N., Cummings, M. J., Brogan, J. F., Hao, L.,
874 Paramonov, M., Hong, J., and Prisle, N. L.: Adsorptive uptake of water by semisolid secondary
875 organic aerosols, *Geophys. Res. Lett.*, 42, 3063-3068, 2015.

876 Park, S. H., Rogak, S. N., and Grieshop, A. P.: A Two-Dimensional Laminar Flow Model for
877 Thermodenuders Applied to Vapor Pressure Measurements, *Aerosol Sci. Technol.*, 47, 283-293,
878 [10.1080/02786826.2012.750711](https://doi.org/10.1080/02786826.2012.750711), 2013.

879 Petters, M., and Kreidenweis, S.: A single parameter representation of hygroscopic growth and



- 880 cloud condensation nucleus activity, *Atmos. Chem. Phys.*, 7, 1961-1971, 2007.
- 881 Petters, M. D., Wex, H., Carrico, C. M., Hallbauer, E., Massling, A., McMeeking, G. R.,
882 Poulain, L., Wu, Z., Kreidenweis, S. M., and Stratmann, F.: Towards closing the gap between
883 hygroscopic growth and activation for secondary organic aerosol – Part 2: Theoretical approaches,
884 *Atmos. Chem. Phys.*, 9, 3999-4009, 10.5194/acp-9-3999-2009, 2009.
- 885 Petters, M., and Kreidenweis, S.: A single parameter representation of hygroscopic growth and
886 cloud condensation nucleus activity–Part 3: Including surfactant partitioning, *Atmos. Chem. Phys.*,
887 13, 1081-1091, 2013.
- 888 Philippin, S., Wiedensohler, A., and Stratmann, F.: Measurements of non-volatile fractions of
889 pollution aerosols with an eight-tube volatility tandem differential mobility analyzer (VTDMA-8),
890 *J. Aerosol Sci.*, 35, 185-203, <http://dx.doi.org/10.1016/j.jaerosci.2003.07.004>, 2004.
- 891 Qin, Y. M., Tan, H. B., Li, Y. J., Schurman, M. I., Li, F., Canonaco, F., Prévôt, A. S. H., and
892 Chan, C. K.: The role of traffic emissions in particulate organics and nitrate at a downwind site in
893 the periphery of Guangzhou, China, *Atmos. Chem. Phys.*, 1-31, 2017.
- 894 Rastak, N., Pajunoja, A., Acosta Navarro, J. C., Ma, J., Song, M., Partridge, D. G., Kirkevåg,
895 A., Leong, Y., Hu, W. W., Taylor, N. F., Lambe, A., Cerully, K., Bougiatioti, A., Liu, P., Krejci, R.,
896 Petäjä, T., Percival, C., Davidovits, P., Worsnop, D. R., Ekman, A. M. L., Nenes, A., Martin, S.,
897 Jimenez, J. L., Collins, D. R., Topping, D. O., Bertram, A. K., Zuend, A., Virtanen, A., and Riipinen,
898 I.: Microphysical explanation of the RH-dependent water affinity of biogenic organic aerosol and
899 its importance for climate, *Geophys. Res. Lett.*, 44, 5167-5177, 10.1002/2017GL073056, 2017.
- 900 Riipinen, I., Pierce, J. R., Donahue, N. M., and Pandis, S. N.: Equilibration time scales of
901 organic aerosol inside thermodenuders: Evaporation kinetics versus thermodynamics, *Atmos.*
902 *Environ.*, 44, 597-607, <https://doi.org/10.1016/j.atmosenv.2009.11.022>, 2010.
- 903 Rose, D., Nowak, A., Achtert, P., Wiedensohler, A., Hu, M., Shao, M., Zhang, Y., Andreae, M.
904 O., and Pöschl, U.: Cloud condensation nuclei in polluted air and biomass burning smoke near the
905 mega-city Guangzhou, China – Part 1: Size-resolved measurements and implications for the
906 modeling of aerosol particle hygroscopicity and CCN activity, *Atmos. Chem. Phys.*, 10, 3365-3383,
907 10.5194/acp-10-3365-2010, 2010.
- 908 Saha, P. K., Khlystov, A., Grieshop, A. P.: Determining aerosol volatility parameters using a



- 909 “Dual Thermodenuder” system: application to laboratory-generated organic aerosols, *Aerosol Sci.*
910 *Tech.*, 49, 620-632, 2015.
- 911 Saha, P. K., Khlystov, A., Yahya, K., Zhang, Y., Xu, L., Ng, N. L., Grieshop, A. P.: Quantifying
912 the volatility of organic aerosol in the southeastern US, *Atmos. Chem. Phys.*, 17, 501-520, 2017.
- 913 Saleh, R., Walker, J., and Khlystov, A.: Determination of saturation pressure and enthalpy of
914 vaporization of semi-volatile aerosols: The integrated volume method, *J. Aerosol Sci.*, 39, 876-887,
915 <https://doi.org/10.1016/j.jaerosci.2008.06.004>, 2008.
- 916 Seinfeld, J. H., and Pandis, S. N.: *Atmospheric chemistry and physics: from air pollution to*
917 *climate change*, John Wiley & Sons, 2016.
- 918 Shrivastava, M., Cappa, C. D., Fan, J., Goldstein, A. H., Guenther, A. B., Jimenez, J. L., Kuang,
919 C., Laskin, A., Martin, S. T., Ng, N. L., Petaja, T., Pierce, J. R., Rasch, P. J., Roldin, P., Seinfeld, J.
920 H., Shilling, J., Smith, J. N., Thornton, J. A., Volkamer, R., Wang, J., Worsnop, D. R., Zaveri, R. A.,
921 Zelenyuk, A., and Zhang, Q.: Recent advances in understanding secondary organic aerosol:
922 Implications for global climate forcing, *Rev. Geophys.*, 55, 509-559,
923 <https://doi.org/10.1002/2016RG000540>, 2017.
- 924 Stokes, R., and Robinson, R.: Interactions in aqueous nonelectrolyte solutions. I. Solute-
925 solvent equilibria, *J. Phys. Chem.*, 70, 2126-2131, 1966.
- 926 Stolzenburg, M. R., and McMurry, P. H.: Equations Governing Single and Tandem DMA
927 Configurations and a New Lognormal Approximation to the Transfer Function, *Aerosol Sci. Tech.*,
928 42, 421-432, [10.1080/02786820802157823](https://doi.org/10.1080/02786820802157823), 2008.
- 929 Sun, Y. L., Zhang, Q., Schwab, J. J., Yang, T., Ng, N. L., and Demerjian, K. L.: Factor analysis
930 of combined organic and inorganic aerosol mass spectra from high resolution aerosol mass
931 spectrometer measurements, *Atmos. Chem. Phys.*, 12, 8537-8551, [10.5194/acp-12-8537-2012](https://doi.org/10.5194/acp-12-8537-2012),
932 2012.
- 933 Tan, H., Xu, H., Wan, Q., Li, F., Deng, X., Chan, P. W., Xia, D., and Yin, Y.: Design and
934 Application of an Unattended Multifunctional H-TDMA System, *J. Atmos. Oceanic Tech.*, 30, 1136-
935 1148, [10.1175/JTECH-D-12-00129.1](https://doi.org/10.1175/JTECH-D-12-00129.1), 2013a.
- 936 Tan, H., Yin, Y., Gu, X., Li, F., Chan, P. W., Xu, H., Deng, X., and Wan, Q.: An observational
937 study of the hygroscopic properties of aerosols over the Pearl River Delta region, *Atmos. Environ.*,



- 938 77, 817-826, <http://dx.doi.org/10.1016/j.atmosenv.2013.05.049>, 2013b.
- 939 Thalman, R., Sá, S. S. d., Palm, B. B., Barbosa, H. M., Pöhlker, M. L., Alexander, M. L., Brito,
940 J., Carbone, S., Castillo, P., Day, D. A.: CCN activity and organic hygroscopicity of aerosols
941 downwind of an urban region in central Amazonia: seasonal and diel variations and impact of
942 anthropogenic emissions, *Atmos. Chem. Phys.*, 17, 11779-11801, 2017.
- 943 Ulbrich, I. M., Canagaratna, M. R., Zhang, Q., Worsnop, D. R., and Jimenez, J. L.:
944 Interpretation of organic components from Positive Matrix Factorization of aerosol mass
945 spectrometric data, *Atmos. Chem. Phys.*, 9, 2891-2918, [10.5194/acp-9-2891-2009](https://doi.org/10.5194/acp-9-2891-2009), 2009.
- 946 Volkamer, R., Jimenez, J. L., Martini, F. S., Dzepina, K., Qi, Z., Salcedo, D., Molina, L. T.,
947 Worsnop, D. R., and Molina, M. J.: Secondary organic aerosol formation from anthropogenic air
948 pollution: Rapid and higher than expected, *Geophys. Res. Lett.*, 33, 254-269, 2006.
- 949 Wang, D. S., and Hildebrandt Ruiz, L.: Chlorine-initiated oxidation of n-alkanes under high-
950 NO_x conditions: insights into secondary organic aerosol composition and volatility using a
951 FIGAERO-CIMS, *Atmos. Chem. Phys.*, 18, 15535-15553, [10.5194/acp-18-15535-2018](https://doi.org/10.5194/acp-18-15535-2018), 2018.
- 952 Wang, J., Lee, Y. N., Daum, P. H., Jayne, J., and Alexander, M. L.: Effects of aerosol organics
953 on cloud condensation nucleus (CCN) concentration and first indirect aerosol effect, *Atmos. Chem.*
954 *Phys.*, 8, 6325-6339, [10.5194/acp-8-6325-2008](https://doi.org/10.5194/acp-8-6325-2008), 2008.
- 955 Wang, J., Cubison, M., Aiken, A., Jimenez, J., and Collins, D.: The importance of aerosol
956 mixing state and size-resolved composition on CCN concentration and the variation of the
957 importance with atmospheric aging of aerosols, *Atmos. Chem. Phys.*, 10, 7267-7283, 2010.
- 958 Wu, Z. J., Poulain, L., Henning, S., Dieckmann, K., Birmili, W., Merkel, M., van Pinxteren,
959 D., Spindler, G., Müller, K., Stratmann, F., Herrmann, H., and Wiedensohler, A.: Relating particle
960 hygroscopicity and CCN activity to chemical composition during the HCCT-2010 field campaign,
961 *Atmos. Chem. Phys.*, 13, 7983-7996, [10.5194/acp-13-7983-2013](https://doi.org/10.5194/acp-13-7983-2013), 2013.
- 962 Xu, W., Chen, C., Qiu, Y., Xie, C., Chen, Y., Ma, N., Xu, W., Fu, P., Wang, Z., Pan, X., Zhu, J.,
963 Ng, N. L., and Sun, Y.: Size-resolved characterization of organic aerosol in the North China Plain:
964 new insights from high resolution spectral analysis, *Environ. Sci. Atmos.*, 1, 346-358,
965 [10.1039/D1EA00025J](https://doi.org/10.1039/D1EA00025J), 2021.
- 966 Xu, W., Xie, C., Karnezi, E., Zhang, Q., Wang, J., Pandis, S. N., Ge, X., Zhang, J., An, J., Wang,



967 Q., Zhao, J., Du, W., Qiu, Y., Zhou, W., He, Y., Li, Y., Li, J., Fu, P., Wang, Z., Worsnop, D. R., and
968 Sun, Y.: Summertime aerosol volatility measurements in Beijing, China, *Atmos. Chem. Phys.*, 19,
969 10205-10216, 10.5194/acp-19-10205-2019, 2019.

970 Yuan, L., Zhang, X., Feng, M., Liu, X., Che, Y., Xu, H., Schaefer, K., Wang, S., and Zhou, Y.:
971 Size-resolved hygroscopic behaviour and mixing state of submicron aerosols in a megacity of the
972 Sichuan Basin during pollution and fireworks episodes, *Atmos. Environ.*, 226, 117393,
973 <https://doi.org/10.1016/j.atmosenv.2020.117393>, 2020.

974 Zdanovskii, A.: NOVYI METOD RASCHETA RASTVORIMOSTEI ELEKTROLITOV V
975 MNOGOKOMPONENTNYKH SISTEMAKH. 1, *Zhurnal Fizicheskoi Khimii*, 22, 1478-1485,
976 1948.

977 Zhang, Q., Canagaratna, M. R., Jayne, J. T., Worsnop, D. R., and Jimenez, J. L.: Time-and size-
978 resolved chemical composition of submicron particles in Pittsburgh: Implications for aerosol
979 sources and processes, *J. Geophys. Res. Atmos.*, 1984–2012, 110, 2005a.

980 Zhang, Q., Worsnop, D. R., Canagaratna, M. R., and Jimenez, J. L.: Hydrocarbon-like and
981 oxygenated organic aerosols in Pittsburgh: insights into sources and processes of organic aerosols,
982 *Atmos. Chem. Phys.*, 5, 3289-3311, 10.5194/acp-5-3289-2005, 2005b.

983 Zhang, Y., Tao, J., Ma, N., Kuang, Y., Wang, Z., Cheng, P., Xu, W., Yang, W., Zhang, S., Xiong,
984 C., Dong, W., Xie, L., Sun, Y., Fu, P., Zhou, G., Cheng, Y., and Su, H.: Predicting cloud condensation
985 nuclei number concentration based on conventional measurements of aerosol properties in the North
986 China Plain, *Sci. Tot. Environ.*, 719, 137473, <https://doi.org/10.1016/j.scitotenv.2020.137473>, 2020.

987 Zhao, D. F., Buchholz, A., Kortner, B., Schlag, P., Rubach, F., Kiendler-Scharr, A., Tillmann,
988 R., Wahner, A., Flores, J. M., Rudich, Y., Watne, Å. K., Hallquist, M., Wildt, J., and Mentel, T. F.:
989 Size-dependent hygroscopicity parameter (κ) and chemical composition of secondary organic cloud
990 condensation nuclei, *Geophys. Res. Lett.*, 42, 920-910, 928,
991 <https://doi.org/10.1002/2015GL066497>, 2015.

992 Zhao, D. F., Buchholz, A., Kortner, B., Schlag, P., Rubach, F., Fuchs, H., Kiendler-Scharr, A.,
993 Tillmann, R., Wahner, A., Watne, Å. K., Hallquist, M., Flores, J. M., Rudich, Y., Kristensen, K.,
994 Hansen, A. M. K., Glasius, M., Kourtchev, I., Kalberer, M., and Mentel, T. F.: Cloud condensation
995 nuclei activity, droplet growth kinetics, and hygroscopicity of biogenic and anthropogenic



996 secondary organic aerosol (SOA), Atmos. Chem. Phys., 16, 1105-1121, 10.5194/acp-16-1105-2016,
997 2016.
998



999 Table 1. The density and the κ value of the related species used in this study.

Species	Density (kg m^{-3})	κ
NH_4NO_3	1720 ^a	0.58 ^b
NH_4HSO_4	1780 ^a	0.56 ^b
H_2SO_4	1830 ^a	0.90 ^b
$(\text{NH}_4)_2\text{SO}_4$	1769 ^a	0.48 ^b
Organics	1400 ^a	0.10 ^b
BC	1770 ^c	0 ^d

1000 ^a From Gysel et al. (2007); ^b From (Cai et al., 2018); ^c From Deng et al. (2019); ^d Assumed to be 0.

1001



1002 Table 2. Thermophysical properties of each component used in the multi-component evaporation
1003 dynamics model.

Parameters	ELVOA	LVOA	SVOA	Ammonium	Ammonium	Black
				Nitrate	Sulfate	Carbon
$C_i^*(T_{ref})$ ($\mu\text{g m}^{-3}$) ^a	10^{-5}	10^{-2}	10	76	2×10^{-3}	10^{-30}
D_i ($\text{m}^2 \text{s}^{-1}$) ^b	5×10^{-6}	5×10^{-6}	5×10^{-6}	5×10^{-6}	5×10^{-6}	5×10^{-6}
$\sigma_{s/a}$ (N m^{-1}) ^c	0.05	0.05	0.05	0.05	0.05	0.05
M_i (kg mol^{-1})	0.2	0.2	0.2	0.08	0.132	0.28
ρ_i (kg m^{-3})	1400	1400	1400	1720	1769	1770
$\Delta H_{\text{vap},i}$ (kJ mol^{-1}) ^d	80	80	80	152	94	100
α^c	0.09	0.09	0.09	0.09	0.09	0.09

1004 ^a From Hong et al. (2017); ^b From Riipinen et al. (2010); ^c From Riipinen et al. (2010); ^d The ΔH_{vap}
1005 values of organics are obtained from the sensitivity test shown in Fig. S4 and the values of inorganic
1006 species are from Hong et al. (2017); ^e Obtained from the sensitivity test shown in Fig. S4.
1007



1008 Table 3. The average and standard deviation values (mean \pm std) of N_{CCN} , AR, D_{50} , and κ_{CCN} at 0.1%,
1009 0.2%, 0.4%, 0.7%, 0.9% and 1.0% SS during the campaign.

SS	0.1%	0.2%	0.4%	0.7%	0.9%	1.0%
N_{CCN} (# cm ⁻³)	2507 \pm 1187	4322 \pm 1981	5843 \pm 2461	6834 \pm 2921	7497 \pm 3210	7862 \pm 3352
AR	0.20 \pm 0.09	0.34 \pm 0.13	0.45 \pm 0.16	0.52 \pm 0.17	0.57 \pm 0.17	0.60 \pm 0.17
D_{50} (nm) 26	145.55 \pm 11.	92.83 \pm 8.80	66.79 \pm 6.33	52.56 \pm 5.46	45.38 \pm 4.82	42.26 \pm 4.45
κ_{CCN}	0.48 \pm 0.13	0.47 \pm 0.15	0.31 \pm 0.10	0.22 \pm 0.09	0.20 \pm 0.08	0.20 \pm 0.08

1010



1011 FIGURE CAPTIONS

1012 Figure 1. The temporal profile of the measured variables during the campaign. (a) particle number
1013 size distribution; (b) PM_{10} chemical composition measured by the SP-AMS along with mass
1014 concentration of $PM_{2.5}$; (c) mass fraction of each species; (d) wind speed and direction. The color
1015 code in (d) represents the wind direction.

1016 Figure 2. The temporal profile of GF-PDF at the measured diameters (30, 50, 80, 100, 150 and 200
1017 nm). The color code denotes the probability density and the red solid line represents the mean GF
1018 (GF_{mean}).

1019 Figure 3. The average mass fraction distribution of SVOA, LVOA and ELVOA at the measured
1020 diameters (30, 50, 80, 100, 150 and 200 nm), and average size-resolved hygroscopicity of organic
1021 aerosol (κ_{OA}) with the upper and lower error bars (in red).

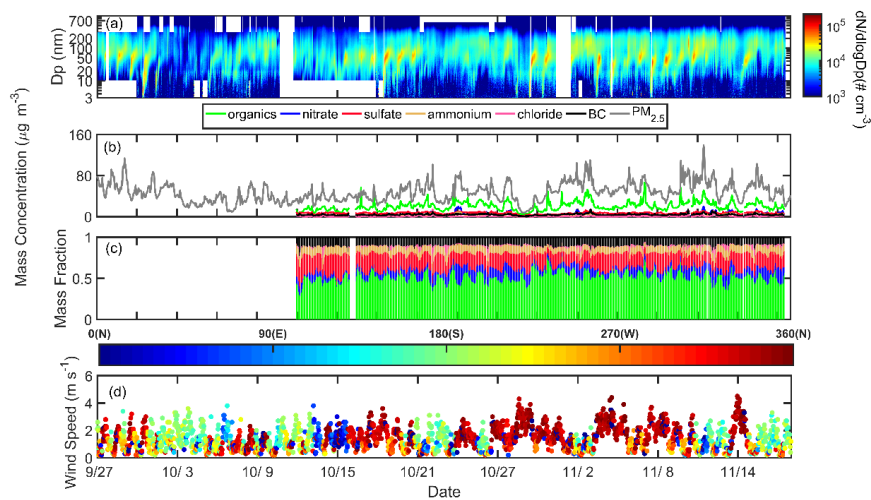
1022 Figure 4. The campaign average diurnal variation of mass fraction of organics and f44 in bulk
1023 PM_{10} (a), the κ values at 200 nm obtained by HTDMA (κ_{HTDMA}) and AMS (κ_{AMS}) measurements
1024 (b), the PNSD (c) and mass distribution of organics (d). The shaded area represents standard
1025 deviation.

1026 Figure 5. The diurnal variation (displayed in boxplot) mass concentration of the deconvolved OA
1027 factors from PMF analysis of AMS data, including more oxygenated OA (MOOA), less
1028 oxygenated OA (LOOA), aged biomass burning OA (aBBOA), hydrocarbon-like OA (HOA),
1029 biomass burning OA (BBOA), and nighttime OA (night-OA).

1030 Figure 6. The average (solid line) and standard deviation (shaded area) diurnal variation of κ_{OA} at
1031 different particle diameters.



1032 Figure 7. The size-resolved volatility distribution during daytime (8:00-16:00 LT) and nighttime
1033 (20:00 to 4:00 LT) based on the median time of each cycle owing to the limited time resolution.
1034 Figure 8. The average diurnal variation of δ_{NCCN} at 0.1%, 0.2%, 0.4% and 0.7% SS based on fixed
1035 κ_{OA} (a), SR κ_{OA} (b) and SR diurnal κ_{OA} (c).
1036



1037

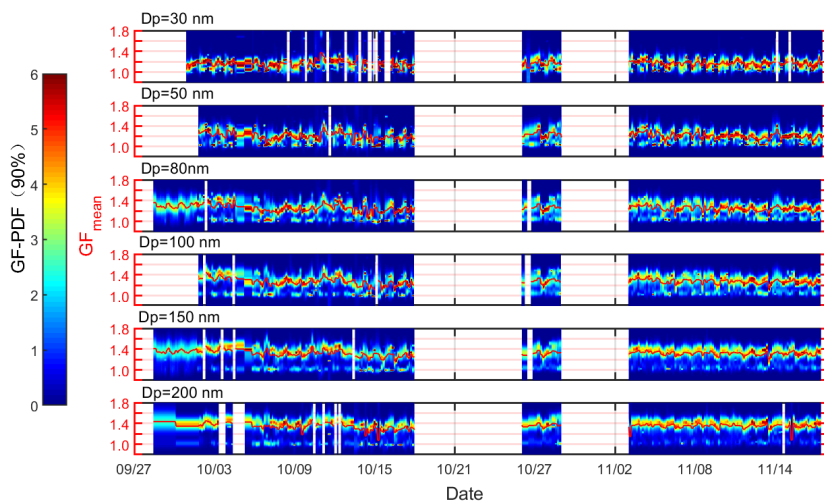
1038

1039

1040

Fig. 1.

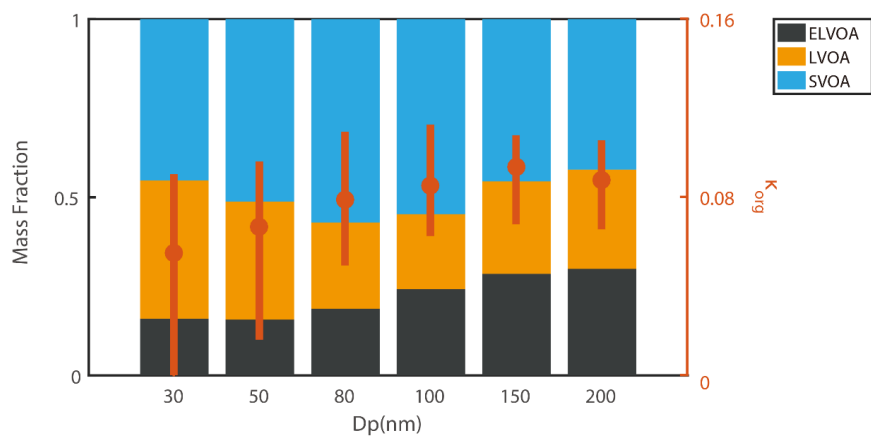
1041



1042

1043 Fig. 2.

1044

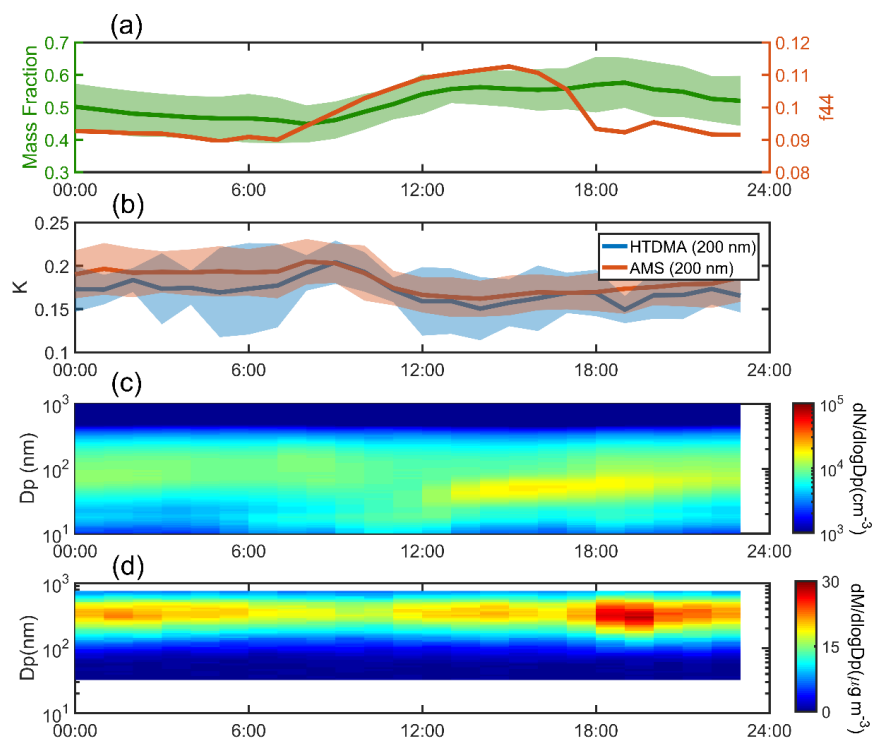


1045

1046

1047 Fig. 3.

1048

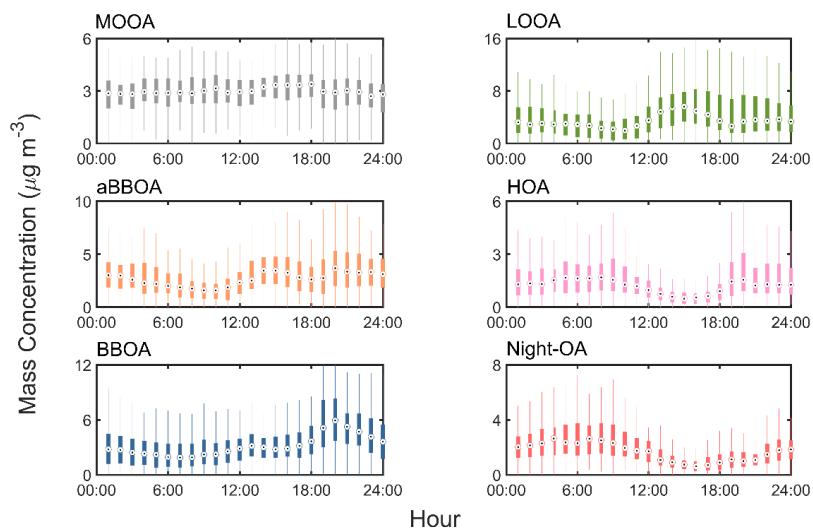


1049

1050

1051 Fig. 4.

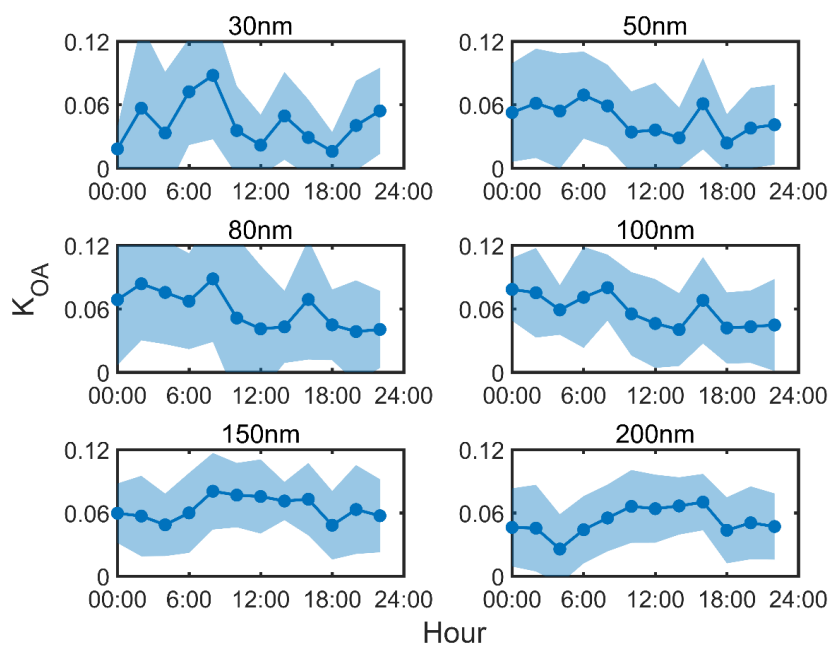
1052



1053

1054

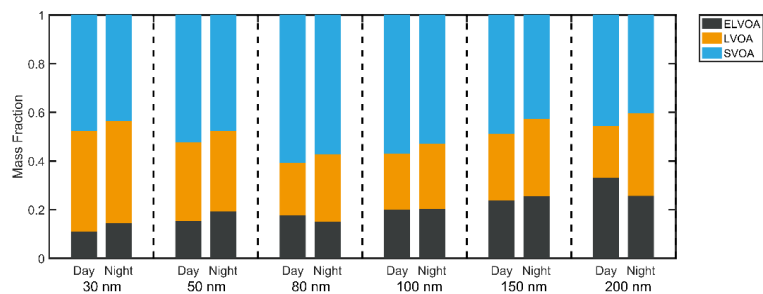
1055 Fig. 5.



1056

1057

1058 Fig. 6.



1059

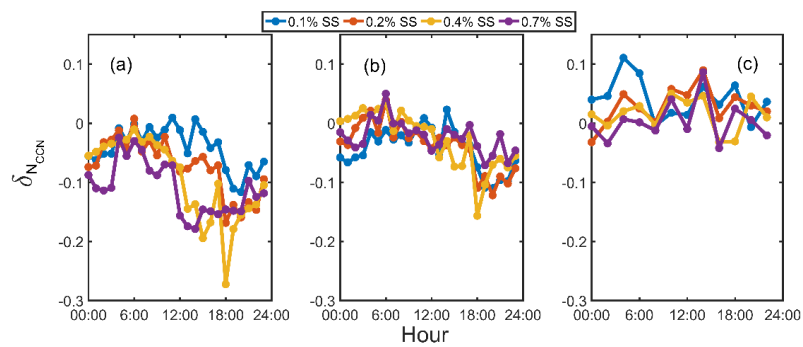
1060

1061 Fig. 7.

1062



1063



1064

1065

1066 Fig. 8.